JOURNAL OF GEOPHYSICAL RESEARCH, VOL. 113, D12110, doi:10.1029/2008JD010026, 2008

General aspects of a T213L256 middle atmosphere general circulation model

Shingo Watanabe,[1] Yoshio Kawatani,[1] Yoshihiro Tomikawa,[2] Kazuyuki Miyazaki,[1] Masaaki Takahashi,[1,3] and Kaoru Sato[4]

Received 26 February 2008; revised 17 April 2008; accepted 25 April 2008; published 25 June 2008.

[1] A high-resolution middle atmosphere general circulation model (GCM) developed for studying small-scale atmospheric processes is presented, and the general features of the model are discussed. The GCM has T213 spectral horizontal resolution and 256 vertical levels extending from the surface to a height of 85 km with a uniform vertical spacing of 300 m. Gravity waves (GWs) are spontaneously generated by convection, topography, instability, and adjustment processes in the model, and the GCM reproduces realistic general circulation in the extratropical stratosphere and mesosphere. The oscillations similar to the stratopause semiannual oscillation and the quasi-biennial oscillation (QBO) in the equatorial lower stratosphere are also spontaneously generated in the GCM, although the period of the QBO-like oscillation is short (15 months). The relative roles of planetary waves, large-scale GWs, and small-scale GWs in maintenance of the meridional structures of the zonal wind jets in the middle atmosphere are evaluated by calculating Eliassen-Palm diagnostics separately for each of these three groups of waves. Small-scale GWs are found to cause deceleration of the wintertime polar night jet and the summertime easterly jet in the mesosphere, while extratropical planetary waves primarily cause deceleration of the polar night jet below a height of approximately 60 km. The meridional distribution and propagation of small-scale GWs are shown to affect the shape of the upper part of mesospheric jets. The phase structures of orographic GWs over the South Andes and GWs emitted from the tropospheric jet stream are discussed as examples of realistic GWs reproduced by the T213L256 GCM.

Citation: Watanabe, S., Y. Kawatani, Y. Tomikawa, K. Miyazaki, M. Takahashi, and K. Sato (2008), General aspects of a T213L256 middle atmosphere general circulation model, *J. Geophys. Res.*, *113*, D12110, doi:10.1029/2008JD010026.

1. Introduction

[2] Since the early 1980s, many atmospheric general circulation models (GCMs) have been developed to support studies of the middle atmosphere [cf. *Pawson et al.*, 2000]. However, as indicated by a comparison of the results of 13 middle atmosphere GCMs with observations by *Pawson et al.* [2000], the accuracy of GCM simulations is generally inhibited by the limited spatial resolution of the model and the many assumptions required for physical parameterization. Nevertheless, GCMs have made substantial contributions to middle atmosphere science, allowing the physical mechanisms responsible for newly discovered phenomena to be investigated, and providing a means of validating newly proposed mechanisms and hypotheses. For example, middle atmosphere GCMs have been used to explain the large gravity wave potential energy observed over the Central Atlantic [*Kawatani et al.*, 2003], and to investigate the downward propagation of solar influence [*Matthes et al.*, 2006]. Many numerical experiments using GCMs have been performed in attempts to evaluate the impacts of known processes affecting atmospheric general circulation, such as the impact of polar ozone depletion on the springtime internal variability of the stratosphere and troposphere [*Watanabe et al.*, 2002], and the impact of the equatorial quasi-biennial oscillation (QBO) on the internal variability of the northern winter [*Naito et al.*, 2003]. Lagrangian transport processes in the middle and upper atmosphere have also been visualized through GCM simulations [e.g., *Kida*, 1983; *Watanabe et al.*, 1999], and complex chemistry-coupled climate models (CCMs) have been developed to understand interactions between chemical compositions and climate [cf. *Eyring et al.*, 2005, 2006].

[3] It is well known that small-scale gravity waves with horizontal wavelengths of tens to hundreds of kilometers play an important role in the general circulation of the middle atmosphere [e.g., *Fritts and Alexander*, 2003]. Gravity waves transport momentum and energy upward

[1]Frontier Research Center for Global Change, Japan Agency for Marine-Earth Science and Technology, Yokohama, Japan.
[2]National Institute of Polar Research, Tokyo, Japan.
[3]Also at Center for Climate System Research, University of Tokyo, Kashiwa, Japan.
[4]Department of Earth and Planetary Science, Graduate School of Science, University of Tokyo, Tokyo, Japan.

0148-0227/08/2008JD010026$09.00

from the troposphere into the middle atmosphere, where the deposition of momentum results in the acceleration of large-scale circulations. In the mesosphere, the upper part of the winter westerly jet (polar night jet) and the summer easterly jet are strongly decelerated by this effect, known as gravity wave drag, which simultaneously induces meridional circulation from the summer pole to the winter pole [*Garcia and Boville*, 1994]. The downward branch of this meridional circulation causes strong dynamical heating on polar temperatures not only in the mesosphere, but also in the upper stratosphere. The accurate reproduction of small-scale gravity waves is therefore particularly important for correctly simulating middle atmosphere zonal wind jets and polar temperatures. However, most existing GCMs and CCMs do not have sufficient horizontal resolution to explicitly reproduce such small-scale gravity waves, necessitating the use of gravity wave drag parameterizations to obtain realistic general circulation [cf. *McLandress*, 1998]. The finest horizontal resolution reported for a simulation covering the entire troposphere, stratosphere, and mesosphere was performed using the N270L40 Geophysical Fluid Dynamics Laboratory (GFDL) "SKYHI" GCM, which has a horizontal resolution of 0.33° and 40 vertical layers [*Hamilton et al.*, 1999]. The SKYHI GCM successfully simulated a realistic Southern Hemisphere polar night jet with better accuracy than by GCMs with lower horizontal resolution, and also afforded realistic horizontal wave number spectra for small-scale motions [*Hamilton et al.*, 1999; *Koshyk et al.*, 1999].

[4] Vertical resolution is also important, particularly when simulating low-latitude circulations such as the QBO [e.g., *Takahashi*, 1996, 1999, *Hamilton et al.*, 1999]. Sufficiently fine vertical resolution is also required in order to simulate the vertical propagation of gravity waves, even those with long vertical wavelengths, since the vertical wavelengths are modified by the background wind shear and static stability variation during propagation. Insufficient vertical resolution therefore leads to artificial dissipation of gravity waves in the vicinity of the critical level for each gravity wave.

[5] Fine vertical resolution is also desirable in order to validate GCM results against observations of gravity waves, and to interpret observed phenomena in reference to GCM results. Radiosonde observations are typically obtained at a vertical resolution of $O(10-100$ m) [e.g., *Allen and Vincent*, 1995; *Sato and Dunkerton*, 1997; *Yoshiki and Sato*, 2000; *Sato et al.*, 2003], and MST (mesospheric–stratospheric–tropospheric) radar and lidar have a vertical resolution of $O(100$ m) [e.g., *Sato and Woodman*, 1982; *Sato*, 1994; *Sato et al.*, 1997; *Wilson et al.*, 1991]. Recent satellite data, such as data acquired by the Microwave Limb Sounder (MLS), Advanced Microwave Sounder Unit (AMSU)-A, Cryogenic Infrared Spectrometers and Telescopes for the Atmosphere (CRISTA), Atmospheric Infrared Sounder (AIRS), High-Resolution Dynamics Limb Sounder (HIRDLS), and Sounding of the Atmosphere using Broadband Emission Radiometry (SABER) instruments and Global Positioning System (GPS) occultation measurements, have a wide range of horizontal and vertical resolution [*Wu and Waters*, 1996; *Wu*, 2004; *Eckermann and Preusse*, 1999; *Ern et al.*, 2004, 2007; *Alexander and Barnett*, 2007; *Alexander et al.*, 2008; *Tsuda et al.*, 2000]. Comparison of GCM simulations with satellite observations therefore requires consideration of the limited range of gravity wave spectra measured by satellite instrumentation [*Alexander*, 1998]. Comparisons of satellite observations with GCM simulations of the global distribution and three-dimensional propagation characteristics of gravity waves are expected to provide valuable information for the development of improved gravity wave drag parameterizations for use with lower-resolution GCMs and CCMs.

[6] The use of high-resolution GCMs also has the potential to discover new atmospheric phenomena and physical processes previously unseen in observations. For example, using an aqua-planet model with T106 spectral triangular truncation (horizontal) and 53 vertical levels (i.e., T106L53) without gravity wave parameterizations, *Sato et al.* [1999] pointed out a number of new features of gravity waves that were later confirmed by observations. The T106L53 model employed has a vertical spacing of 600 m at heights in the range of 10–30 km, and a horizontal resolution of approximately 120 km. The model realistically simulated the amplitudes and phase structure of monochromatic gravity waves with wave frequency close to the inertial frequency, as detected by MST radar at middle latitudes [*Sato et al.*, 1997]. Spectral analysis of the simulation data indicated that such gravity waves are dominant in the lower stratosphere at all latitudes with weak mean wind, and this feature was later confirmed by ST radar and radiosonde observations [*Nastrom and Eaton*, 2006; *Sato and Yoshiki*, 2008]. The vertical energy fluxes estimated from the simulation also suggested that gravity waves propagating energy downward are dominant in the winter stratosphere, indicating that the polar night jet in the stratosphere is an important gravity wave source in that region. The existence of gravity waves propagating energy downward in the stratosphere was also later confirmed by radiosonde observations [*Yoshiki and Sato*, 2000; *Sato*, 2000; *Yoshiki et al.*, 2004; *Sato and Yoshiki*, 2008].

[7] It is in this context that our group has undertaken the development of a middle atmosphere GCM with increased vertical resolution and high horizontal resolution in order to resolve wave mean flow interactions associated with gravity waves. The proposed GCM covers a region that extends from the surface to a height of approximately 85 km, and is partitioned into 250 vertical layers with uniform vertical resolution of 300 m throughout the middle atmosphere. A 250-layer GCM (T63L250) simulation by *Watanabe and Takahashi* [2005] successfully reproduced spontaneously QBO-like oscillation and stratopause semiannual oscillation (S-SAO) along with the realistic vertical wind shears, through which equatorial Kelvin waves were found to propagate. In a subsequent study, *Watanabe et al.* [2006] successfully resolved gravity waves excited by surface katabatic flows on the west coast of the Ross Sea using a 250-layer GCM with higher horizontal resolution (T213L250). The benefits of finer horizontal resolution have been reported by *Kawamiya et al.* [2005] on the basis of a comparison of T106L250 and T213L250 model results (discussed in section 4).

[8] The aim of the KANTO project to which the present study contributes is to acquire, through the development of a high-resolution GCM, a quantitative understanding of small-scale physical processes such as gravity waves,

trapped Rossby waves, inertial instabilities, fine structure in the vicinity of the tropopause, and layered and filamentary tracer structures, and to elucidate the roles of such phenomena in the large-scale structure, circulations, and oscillations of the middle atmosphere. In development of the GCM employed in the present study, the spatial resolution and other framework settings of the GCM were the first aspects to be considered. In order to perform simulations for a sufficiently long period, the T213 horizontal resolution has not been increased. The 250 vertical layers have been increased marginally to 256 in order to improve computational efficiency. This T213L256 GCM was run on the Earth Simulator for a simulation period of 3 years, encompassing two cycles of spontaneously generated QBO-like oscillation. Gravity wave drag parameterizations are not applied in the present study, and hence all of the gravity waves reproduced by the GCM are generated spontaneously by convection, topography, instability, and adjustment processes in the model.

[9] The main objective of the present work is to report the general characteristics of the T213L256 GCM. Details of the model framework are presenting in section 2. The results for the zonal mean fields and mean precipitation are compared with observations in sections 3.1 and 3.2, and the zonal phase speeds of synoptic-scale disturbances in the extratropical upper troposphere are validated with respect to global reanalysis data in section 3.3. In section 3.4, horizontal wave number spectra of horizontal kinetic energy are compared with the results obtained using other GCMs. The results for the equatorial zonal mean zonal wind are discussed in section 3.5, and the Eliassen-Palm (E-P) flux is analyzed in section 3.6 in order to quantify the wave mean flow interactions associated with planetary-scale waves, synoptic-scale waves, and small-scale gravity waves. The latitudinal distribution and meridional propagation of gravity waves are investigated in section 3.7, and examples of typical gravity waves events produced by the GCM are reported in section 3.8. The results are discussed in section 4, and the study is concluded in section 5.

2. Model Description

[10] The T213L256 middle atmosphere GCM developed in the present study is based on the atmospheric component of version 3.2 of the Model for Interdisciplinary Research on Climate (MIROC), a coupled atmosphere–ocean GCM developed collaboratively by the Center for Climate System Research (CCSR) at the University of Tokyo, the National Institute for Environmental Studies (NIES), and the Frontier Research Center for Global Change (FRCGC) [*K-1 Model Developers*, 2004; *Nozawa et al.*,. 2007]. The atmospheric GCM has been referred to in previous studies as the CCSR/NIES AGCM and CCSR/NIES/FRCGC AGCM [e.g., *Takahashi*, 1996, 1999; *Sato et al.*, 1999; *Kawatani et al.*, 2003, 2004, 2005; *Watanabe and Takahashi*, 2005; *Watanabe et al.*, 2005, 2006]. While developing the middle atmosphere GCM considered in the present study, many parts of the model setup have been modified and extended from those defined in MIROC 3.2. Each of these modifications is described in detail below, and the parameterized subgrid processes are specified, which are important for reproducing the spontaneous generation and dissipation of gravity waves.

2.1. Resolution and Vertical Domain

[11] The present GCM has a horizontal triangularly truncated spectral resolution of T213, corresponding to a latitude-longitude grid interval of 0.5625° (62.5 km near the equator), and comprises 256 vertical layers from the surface to a height of approximately 85 km with a vertical resolution of 300 m throughout the middle atmosphere. The thickness of the vertical layers is reduced within the surface boundary layer, increased to about 750 m in the midtroposphere, and reduced to 300 m in the upper troposphere. The slightly coarse vertical resolution in the midtroposphere is necessary in order to obtain realistic convective precipitation using the Arakawa-Schubert cumulus parameterization. Although the T213 horizontal resolution is insufficient to resolve very small scale, i.e., O(10 km), gravity waves, the vertical resolution is sufficiently fine to resolve the majority of observed gravity waves with acceptable accuracy. High vertical resolution is important when studying the various features of gravity waves, such as modification of the wave structure by background wind shear and static stability variations, critical level filtering, and wave–wave interactions. High vertical resolution is also one of the necessary conditions for spontaneous generation of QBO-like phenomena [*Takahashi*, 1996, 1999; *Baldwin et al.*, 2001; *Watanabe and Takahashi*, 2005; *Kawatani et al.*, 2005].

2.2. Vertical Coordinate System

[12] In the present study, a terrain following σ-vertical coordinate system used in MIROC 3.2 is replaced with a hybrid σ-pressure coordinate system [*Watanabe et al.*, 2008], by which the terrain-following coordinate system gradually transforms into a pressure coordinate system in the troposphere. The pressure coordinate system starts at approximately 350 hPa.

2.3. Trace Constituents and Tracer Advection Scheme

[13] Water vapor and liquid cloud water are defined as prognostic variables, and a climatological or uniform distribution is applied for other trace constituents in the radiation calculations. As the methane oxidation process, which is a primary process of water vapor production in the middle atmosphere, is not considered, the water vapor concentration in the middle atmosphere will be considerably underestimated. Care therefore needs to be taken regarding a possible shortage of infrared (IR) cooling in the middle atmosphere, which leads to warmer (>+5 K) stratopause temperatures in the GCM. The tracer advection scheme employed in the present GCM is the same as that used in MIROC 3.2, namely the flux-form semi-Lagrangian scheme with the monotonic piecewise parabolic method [*Lin and Rood*, 1996].

2.4. Physical Parameterizations

2.4.1. Radiation

[14] The radiative transfer scheme employed in the present GCM is based on the two-stream discrete ordinate method and a correlated k distribution method. The radiation scheme has recently been updated, and the accuracy of the heating rate calculation has been greatly improved (M.

Sekiguchi and T. Nakajima, The study of the absorption process and its computational optimization in an atmospheric general circulation model, submitted to *Journal of Quantitative Spectroscopy and Radiative Transfer*, 2008). As a result, cold biases around the tropopause have been reduced from about −10 K to −4 K [*Watanabe et al.*, 2008]. The solar (0.2–4.0 μm) and terrestrial (4–100 μm) components of radiation are divided into 9 and 10 bands, respectively, in which 1–7 integration points optimized for the k distribution method are placed. By optimizing the integration points, the accuracy of the heating rate calculation in the middle atmosphere up to 70 km has been improved (Sekiguchi and Nakajima, submitted manuscript, 2008).

[15] The gases considered in the present study are O_2, O_3, and H_2O for solar radiation, and CO_2, CH_4, N_2O, O_3, and H_2O for terrestrial radiation. Globally and vertically uniform concentrations are given for O_2 (21%), CO_2 (345 ppmv), CH_4 (1.7 ppmv), and N_2O (0.3 ppmv). The zonal mean value of the United Kingdom Universities' Global Atmospheric Modeling Programme (UGAMP) monthly O_3 climatology is used in the present study (D. Li and K. P. Shine, UGAMP ozone climatology, British Atmospheric Data Center, 1999, available at http://badc.nerc.ac.uk/data/ugamp-o3-climatology/). The water vapor concentration used in the radiation scheme is that internally calculated in the GCM. The radiative transfer is calculated every 3 h using instantaneous model fields, which include temperature, cloud fraction, cloud water, and water vapor, and changes in solar insolation associated with the solar zenith angle are determined at every time step.

2.4.2. Cumulus Convection

[16] The cumulus parameterization is based on the scheme presented by *Arakawa and Schubert* [1974] and is the same as that used in MIROC 3.2. A prognostic closure is used in the cumulus scheme, in which cloud base mass flux is treated as a prognostic variable. The original Arakawa–Schubert scheme has a characteristic in that convective precipitation becomes more frequent and weak as the horizontal resolution of the GCM increases. To prevent this problem, an empirical cumulus suppression condition is introduced [*Emori et al.*, 2001], by which cumulus convection is suppressed when cloud mean ambient relative humidity is less than a critical value. A critical value of 0.72 is adopted in the present study, which results in suppression of overly frequent precipitation and the generation of moderately organized convective precipitation. The organization of convective precipitation is caused by interaction between the parameterized convection at a grid point with that in the surrounding grid points through grid-scale circulations and moisture transport. The size distribution and lifetime of such multigrid-scale convective cloud clusters in the outgoing long-wave radiation field change dramatically with the critical value.

[17] Parameterized cumulus convection is an important source of internal waves in GCMs [*Horinouchi et al.*, 2003]. *Suzuki et al.* [2006] showed that incorporation of the cumulus suppression condition substantially improves the representation of convectively coupled equatorial waves in the atmospheric GCM in MIROC 3.2, and *Lin et al.* [2006] showed that the T42L20 and T106L56 versions of the atmospheric GCM in MIROC 3.2 accurately simulate convectively coupled equatorial waves. The present T213L256 GCM also reproduces realistic convectively coupled equatorial waves, as well as the short-term variability of convective clouds, such as westward traveling cloud clusters with horizontal scales of 100–1000 km and periods of 1–2 days, and eastward traveling super cloud cluster-like structures with eastward phase speeds of approximately 15 m s^{-1} [cf. *Nakazawa*, 1988]. The characteristics of the present parameterized cumulus convection, and the correspondence between the characteristics of cumulus convection and gravity waves in the GCM, will be detailed in a forthcoming paper.

2.4.3. Large-Scale Condensation

[18] The large-scale condensation scheme is the same as that used in MIROC 3.2. The scheme describes grid-scale condensation and precipitation processes and governs condensational heating, precipitation, cloud fraction, and changes in water vapor and cloud liquid water. As the horizontal resolution increases, the grid-scale condensation becomes a more important source of condensational heating and precipitation in the GCM. More than 80% of the extratropical precipitation and approximately 40% of the tropical precipitation are represented by large-scale condensation in the present simulation (not shown). Hence, grid-scale condensational heating is potentially an important generation mechanism of internal waves in the GCM.

2.4.4. Vertical Diffusion

[19] The level 2 scheme of the turbulence closure model proposed by *Mellor and Yamada* [1974, 1982], as used in MIROC 3.2, is employed in the present GCM for eddy vertical diffusion parameterization. The coefficient for eddy vertical diffusion is dependent on the Richardson number, and this parameterization mainly represents vertical mixing associated with gravity wave breaking due to both convective instability and shearing instability in the GCM. Although the present GCM has fine horizontal and vertical resolutions, such turbulent breakdown processes of gravity waves occur at much finer scales, being represented by horizontal and vertical diffusion parameterizations in the model. The background (minimal value) vertical diffusion coefficient is defined uniformly as 0.1 m^2 s^{-1} for both momentum and heat in the middle atmosphere. An increase in this parameter reduces the amplitudes of gravity waves considerably, whereas a decrease beyond the present value does not have a marked effect on the results.

2.4.5. Dry Convective Adjustment

[20] In the middle atmosphere of the GCM, dry convective adjustment acts to eliminate the gravity wave-associated convective instability that is not suppressed by the vertical diffusion parameterization.

2.4.6. Land Surface Processes

[21] The land surface model in MIROC 3.2, the Minimal Advanced Treatments of Surface Interaction and Runoff (MATSIRO), is replaced with a simple bucket model in order to reduce computational time. Thermal conductance within three soil layers and thermal heat balance at the land surface are accounted for in the present GCM. Changes in the land surface albedo due to ice and snow coverage are predicted. The simple bucket model is employed to model hydrology. Although these simplifications may reduce the accuracy of the results to a certain extent near the surface,

the differences realized in the short-term integration conducted in the present study are not expected to be appreciable.

2.4.7. Internal Gravity Wave Drag

[22] Unlike the standard MIROC 3.2, no parameterization of subgrid gravity waves is used in the present simulations.

2.5. Horizontal Diffusion

[23] The ∇^n hyperviscosity diffusion is used in the present GCM to suppress the effect of extra energies at the largest horizontal wave number. A value of $n = 4$ is employed in the present simulation. The *e*-folding time for the smallest resolved wave is 0.9 days. *Koshyk et al.* [1999] showed that the horizontal wave number spectra of wave energies in most spectral GCMs are highly sensitive to the parameters describing the horizontal diffusion. Unfortunately, appropriate values for such parameters are not given theoretically. Empirical tuning of these parameters is therefore necessary in order to obtain realistic horizontal wave number spectra for wave energies and realistic amplitudes for gravity waves. The amplitudes of gravity waves are also dependent on the generation and dissipation characteristics, which are defined in the physical parameterizations of the GCM. The set of parameters employed in the present simulation were obtained by conducting several sensitivity tests aimed at tuning the parameters of horizontal diffusion, accounting also for the cumulus and vertical diffusion parameterizations. In arriving at suitable parameters, attention was primarily paid to obtaining realistic gravity wave amplitudes in the lower stratosphere [*Sato et al.*, 2003].

2.6. Boundary Conditions

[24] Version 1 of the Atmospheric Model Intercomparison Project (AMIP-I) monthly mean climatology (January 1979 to January 1989) for sea surface temperature (SST) and sea ice distribution is applied at the bottom boundary. Topography data are constructed using the United States Geological Survey (USGS) GTOPO30 surface elevation data set. To avoid unrealistic reflections of waves at the top boundary of the model, a sponge layer with a thickness of 8 km is defined at elevations above 0.01 hPa. The sponge layer consists of 6 levels in which the strength of ∇^4 horizontal diffusion is successively doubled (i.e., 2, 4, 8, 16, 32, and 64 times) with respect to the standard value.

2.7. Initial Condition and Integration

[25] A 1-year T213L250 run was performed prior to finalizing the T213L256 GCM employed for the simulations in the present study. The T213L250 GCM was spun-up using restart data for a T106L250 simulation [*Watanabe et al.*, 2006]. The first T213L250 GCM successfully reproduced the extratropical general circulation in the middle atmosphere [*Kawamiya et al.*, 2005]. The primary difference between the first T213L250 GCM simulation and the present T213L256 GCM is the use of a new radiation scheme that greatly reduces cold biases near the tropical tropopause [cf. *Watanabe et al.*, 2008]. The modest increase to 256 layers in the final model was decided upon as being both sufficient to resolve small-scale gravity waves and to be maximize computational efficiency on the Earth Simulator. The 1 October result of the T213L250 simulation was vertically interpolated into the present L256 vertical coordinates. The final T213L256 GCM was spun-up for 3 months in order to obtain the initial condition on 1 January.

[26] The T213L256 GCM was run on the Earth Simulator for a simulation period of 3 successive years with a time step of 30 s. The major meteorological elements were sampled every hour as hourly averages. Data for the troposphere in the hybrid σ-pressure coordinate system were vertically interpolated to standard pressure levels prior to taking averages. A single meteorological element consists of a $640 \times 320 \times 256$ array in longitude, latitude, and standard pressure level.

[27] The present simulation produces a sudden stratospheric warming in the first simulation year, which will be examined in a separate study. The present study focuses on the periods of January in the second simulation year and July in the first simulation year, both of which display typical observed seasonal evolution of the middle atmosphere general circulation.

3. Results

3.1. Mean Field

[28] Figure 1 compares the zonal mean zonal wind and the zonal mean temperature produced by the present GCM with the Met Office assimilation data (below 1 hPa) [*Swinbank and O'Neill*, 1994] and the 1986 Committee on Space Research (COSPAR) International Reference Atmosphere (CIRA) data (above 1 hPa) [*Fleming et al.*, 1990]. The GCM qualitatively reproduces the observed meridional structure of the zonal mean zonal wind and temperature in both January and July, while the model results are those for specific periods, i.e., January in the second simulation year and July in the first simulation year. In the Northern Hemisphere winter, the maximum westerly jet wind speed occurs at approximately 65°N in the stratosphere, and at close to 35°N in the mesosphere. This separation of the westerly jet is roughly balanced with the polar temperature maximum in the lower mesosphere, although the simulated separation occurs at higher altitude than observed. The simulated zonal mean westerly jet is stronger than observed, and the temperature in the polar lower stratosphere is lower. These results are regarded as realistic considering the large interannual variations in the Northern Hemisphere winter. Representativity of the reference observational data should also be considered; that is, CIRA86 data only averages 3 years including very large interannual variations in the mesospheric temperatures [*Lawrence and Randel*, 1996; *Randel et al.*, 2004]. In the Southern Hemisphere summer, the meridional structure of the summertime easterly wind produced by the GCM is very similar to the observations. The maximum wind speed of the easterly jet speed occurs over a latitude range of 15–20°S in the lower mesosphere, and 40–50°S in the upper mesosphere. The maximum wind speed of the easterly jet in the upper mesosphere ($\approx$75 m s^{-1}) is also consistent with observations. The latitudinally uniform excess in temperatures near the stratopause is primarily caused by underestimation of IR cooling due to water vapor, as mentioned in section 2.3.

[29] In the Southern Hemisphere winter, the simulated structure of the polar night jet is qualitatively similar to the observations. The maximum westerly wind is tilted equa-

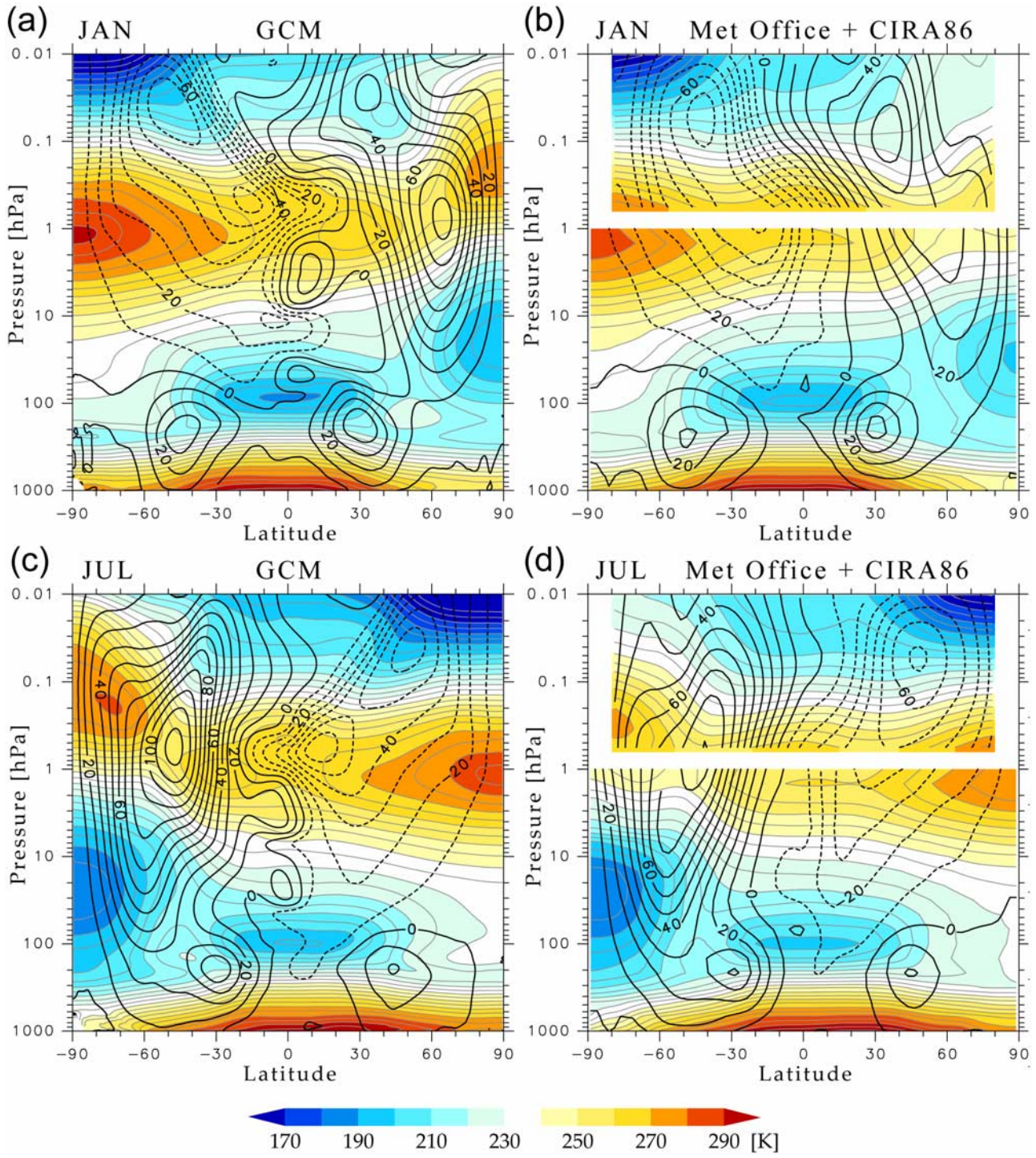

Figure 1. Zonal mean zonal wind (contours) and temperature (color and thin contours) in (a and b) January and (c and d) July. Figures 1a and 1c are for GCM, and Figures 1b and 1d are for Met Office + CIRA86. Contour intervals are 10 m s^{-1} and 5 K. Met Office data are averaged over 1994–2001 and displayed below 1 hPa.

torward with increasing height, from 50 to 60°S in the lower stratosphere to 30–40°S in the upper mesosphere. The maximum wind speed of the polar night jet simulated by the GCM exceeds 120 m s^{-1}, larger than the approximately 100 m s^{-1} indicated by Met Office data. This discrepancy may be due to underestimations of gravity wave drag in the mesosphere of the GCM, as discussed later. In the lower stratosphere, the simulated zonal mean temperature in the polar region is close to the observations, but is slightly underestimated in the upper stratosphere. The wintertime stratopause, determined by the temperature maximum in the polar cap region, is located at higher altitude (0.1–0.2 hPa)

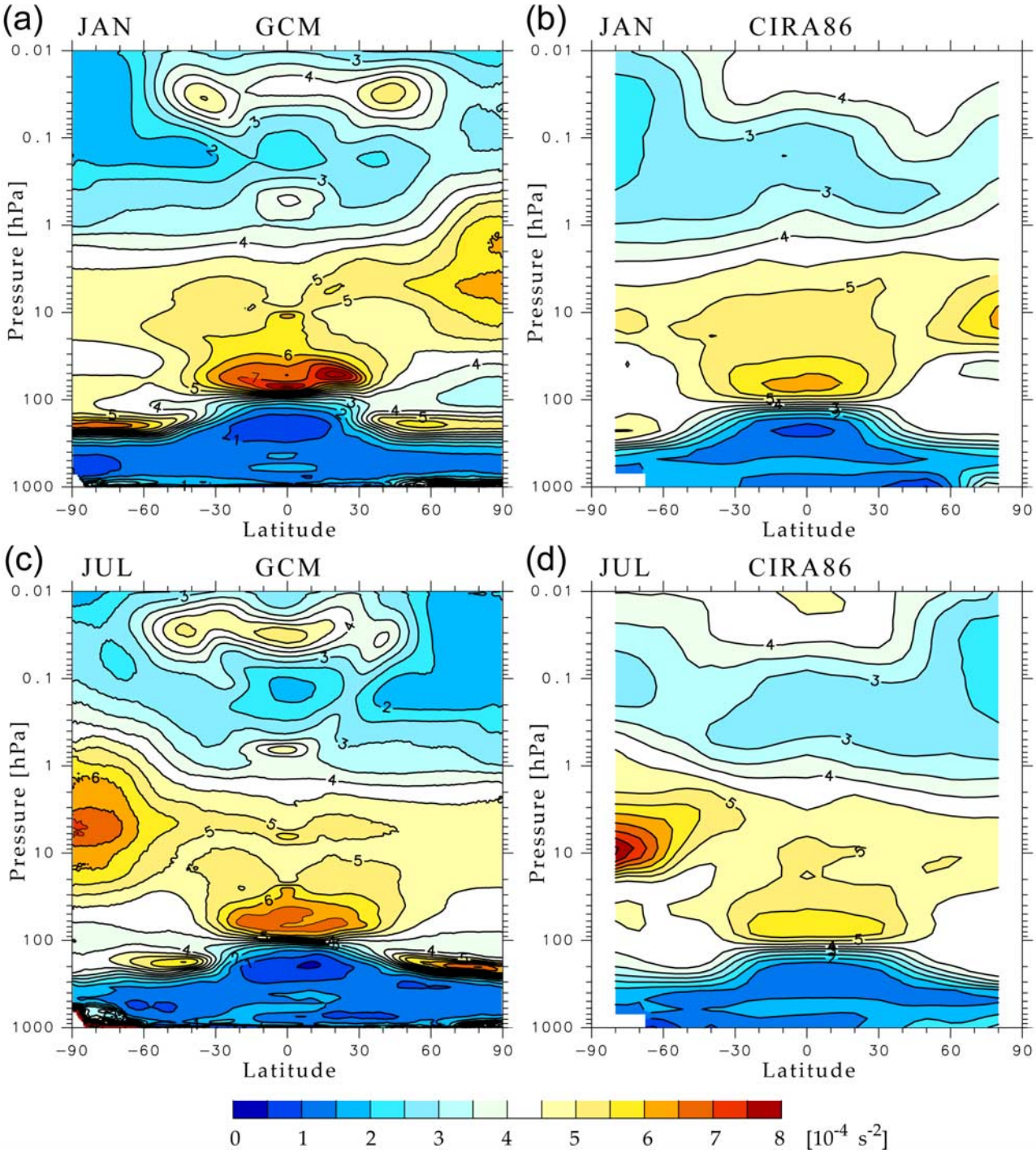

Figure 2. Zonal mean of squared buoyancy frequency (N^2) for (a and b) January and (c and d) July. Figures 2a and 2c are for GCM, and Figures 2b and 2d are for CIRA86. Contour interval is 0.5×10^{-4} s^{-2}.

than indicated by the CIRA temperature data (0.2–0.4 hPa), probably because of underestimation of downwelling in the polar mesosphere, which is driven by gravity wave drag.

[30] In the tropics, the simulated zonal mean zonal winds show a vertically stacked structure of easterlies and westerlies, resembling the QBO in the lower stratosphere and the S-SAO in the upper stratosphere. The vertical structure of the equatorial zonal wind and its evolution are described in section 3.5.

[31] The meridional distribution of the stratopause temperature maximum is interesting. The maximum occurs at around 1 hPa from the summer pole to the equator side of the polar night jet, and within the polar night jet at higher altitudes. The stratopause temperature in the polar night region is primarily controlled by dynamical heating associated with large-scale descent, which is mainly driven by gravity wave drag in the mesosphere [*Hitchman et al.*, 1989]. Hence, the maximum temperature and altitude of

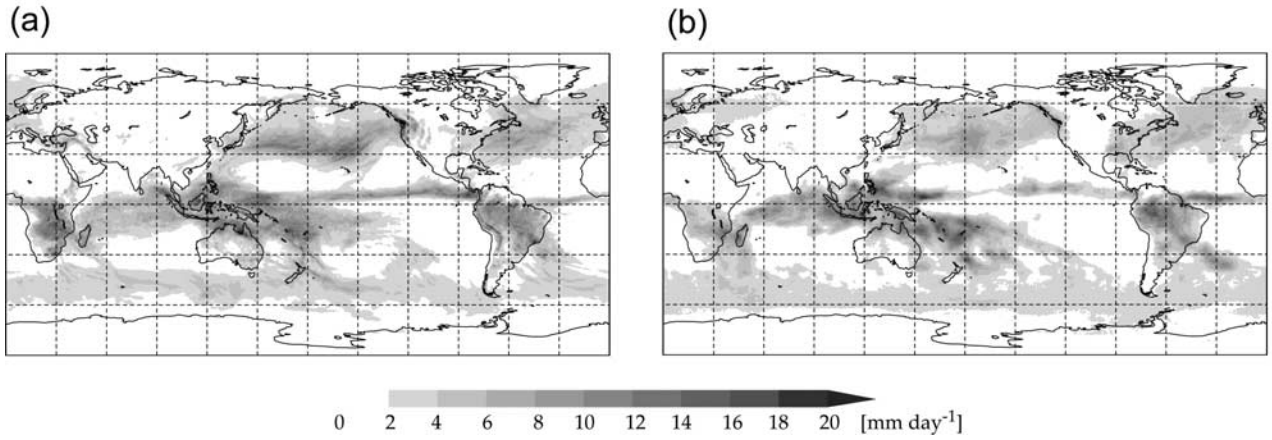

Figure 3. January mean precipitation for the (a) GCM and (b) GPCP in 1999.

the stratopause vary considerably with changes in gravity wave drag. The seasonal variations in large-scale meridional circulations and thermal structures in the GCM will be investigated in detail in future studies in the context of gravity wave effects. Another interesting point is the occurrence of a distinct stratopause temperature maximum at 20–30° latitude in the winter hemisphere in both seasons, corresponding to the region of the equatorward edge of the polar night jet. A similar maximum in stratopause temperature is present in CIRA86, although not apparent in the Met Office data. A companion paper proposes a dynamical mechanism maintaining such a temperature maximum [*Tomikawa et al.*, 2008].

[32] Figure 2 shows the zonal mean of the squared Brunt-Väisälä frequency (N^2) in January and July. The GCM results generally agree well with those calculated using CIRA86 temperatures. A distinct maximum in N^2 occurs above the extratropical tropopause, similar to that indicated by radiosonde observations [e.g., *Birner*, 2006]. A similar enhancement of N^2 is also found above the tropical tropopause in the GCM. In the present study, the tropopause is defined by a contour line of 2.5×10^{-4} s^{-2}, which is close to the position defined by the temperature lapse rate and potential vorticity. The tropopause is located near 100 hPa at low latitudes, and 200–300 hPa in the extratropics.

[33] In the tropics, small structures of N^2 are apparent in the vertical direction, associated with the simulated QBO-like oscillation, the S-SAO, and an intraseasonal oscillation in the mesosphere. In the middle stratosphere, the maximum in N^2 occurs within the polar vortex, reflecting a strong increase in temperature with height above the temperature minimum in the polar lower stratosphere (see Figure 1). The N^2 value is generally larger in the winter hemisphere than in the summer hemisphere, except in the extratropical lowermost stratosphere. The value also decreases above the stratopause, which can be approximated by a 3.5×10^{-4} s^{-2} contour line, that is, 1–2 hPa in the summer hemisphere and about 0.3 hPa at high latitudes in the winter hemisphere. The upper mesospheric structure of the simulated N^2 field is more complex than the observed structure, probably because of intraseasonal oscillation of the zonal mean zonal wind (see Figure 7).

3.2. Precipitation

[34] Figure 3 shows the horizontal distribution of monthly mean precipitation in January. The precipitation simulated by the GCM during January of the second simulation year is compared to the 1999 1° daily data set of the Global Precipitation Climatology Project (GPCP) [*Huffman et al.*, 2001]. The January precipitation in 1999 was typical, and did not correspond to extremes of the El Niño southern oscillation (ENSO). The simulated precipitation is qualitatively similar to the observations, except for a considerable excess around the intertropical convergence zone (ITCZ), Africa, and at middle latitudes. The heavy precipitation in the North Pacific is associated with the interannual variability of the model, and is not observed in other simulation years.

[35] Figure 4 shows the zonal average of the monthly mean precipitation in January. The GCM result is compared to GPCP data for 1997, 1999–2002, and 2004–2006 so as to exclude ENSO extremes. The GCM overestimates the zonal mean precipitation near the equator and at mid latitudes in both hemispheres, but by less than 1σ.

3.3. Disturbances in the Extratropical Upper Troposphere

[36] Figures 5a and 5b show zonal wave number–frequency spectra for a 300 hPa geopotential height at 45°N in January. A simple two-dimensional fast Fourier transformation (FFT) is used to obtain these spectra, with a cos20° window applied at the both ends of the record. The GCM output is compared with the ERA40 reanalysis data for the 1990s [*Uppala et al.*, 2005]. Eastward traveling waves with zonal wave numbers of s = 4–6 and ground-based phase speed of +2 to +10 m s^{-1} are dominant in both the GCM and ERA40 spectra. The distinct peaks for $s = \pm 3$ in the GCM spectra correspond to the enhancement of s = 3 quasi-stationary planetary waves associated with a strong blocking event that occurred in this period (not shown). At larger zonal wave numbers (s = 6–10), eastward traveling waves with larger zonal phase speed (+10 to +20 m s^{-1}) are dominant in the ERA40 data. The corresponding spectral peaks are absent in the GCM, probably because of the development of a planetary wave affecting synoptic- and sub-synoptic-scale weather disturbances. Figures 5c and 5d

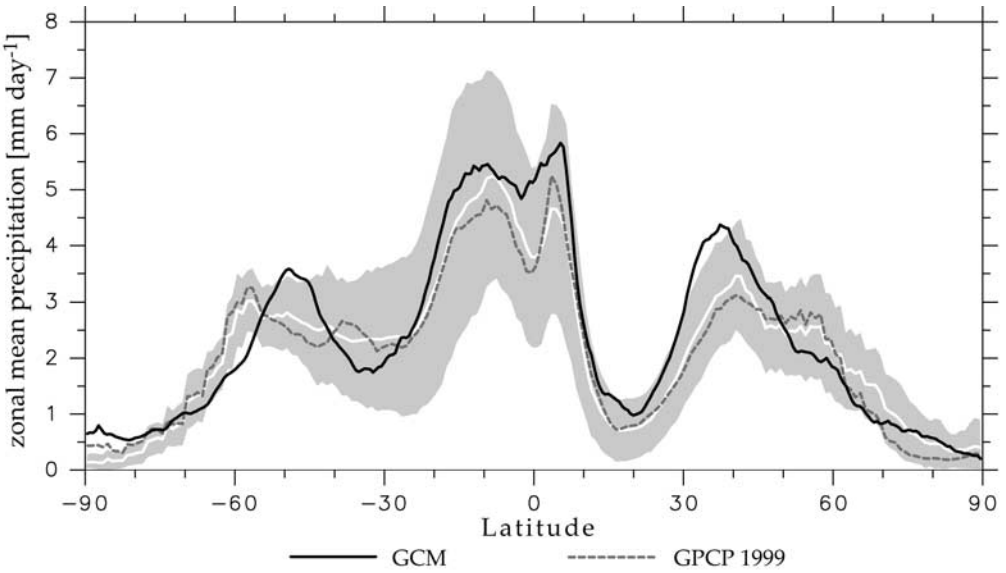

Figure 4. Zonal averages of monthly mean precipitation in January. White line denotes GPCP average for 1997–2006 (excluding 1998 and 2003), and shaded area denotes $\pm 1\sigma$ range of the GPCP data.

show the corresponding spectra calculated at 48°S. A peak corresponding to the $s = 4$ eastward traveling baroclinic waves with small zonal phase speed ($\approx$+5 m s^{-1}) is pronounced in both the GCM and ERA40 spectra. At larger zonal wave numbers ($s = 6$–10), the eastward traveling waves dominant in the GCM spectra have larger zonal phase speeds (+10 to +20 m s^{-1}) than those in the ERA40 spectra (+5 to +15 m s^{-1}). This discrepancy is considered to be due

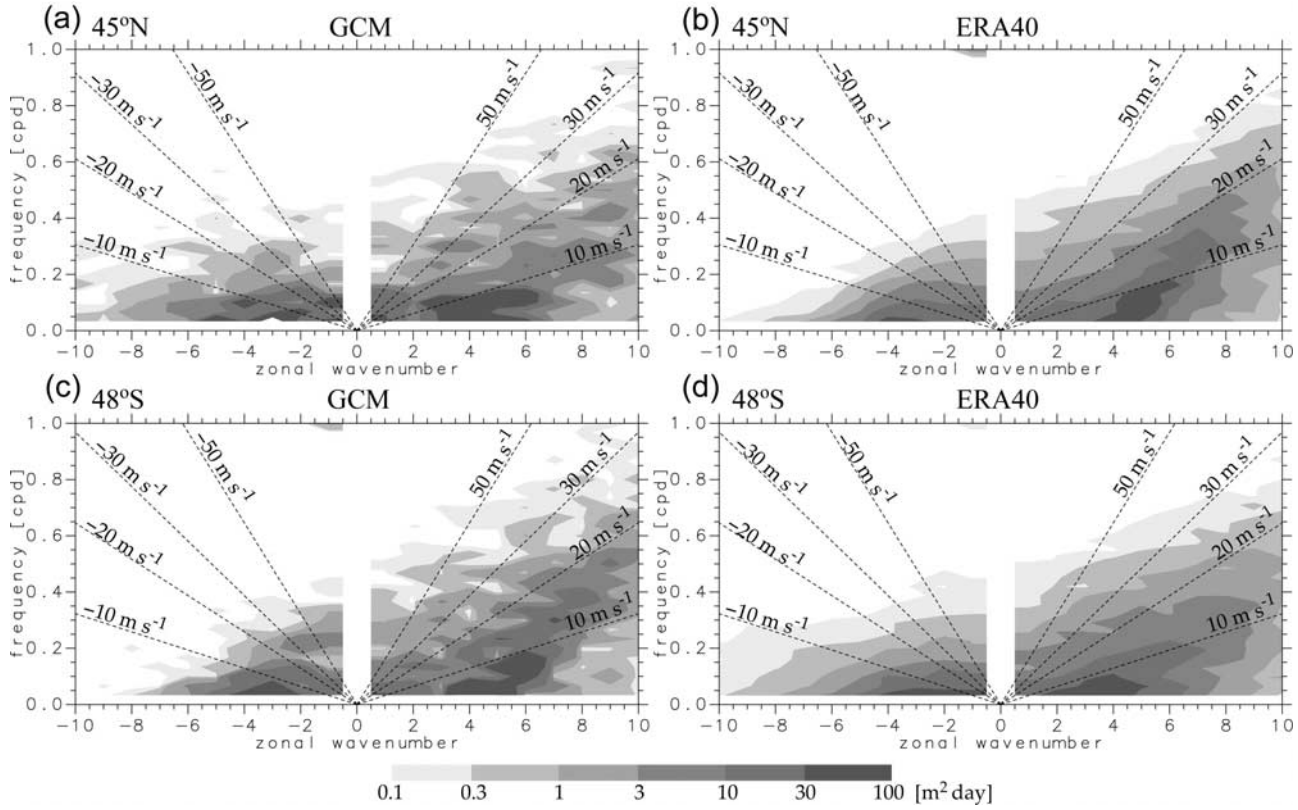

Figure 5. Zonal wave number versus frequency spectra for 300 hPa geopotential height for January. (a and b) 45°N, (c and d) 48°S. Figures 5a and 5c are for GCM, and Figures 5b and 5d are for ERA40. Spectra for ERA40 data are averaged over 1990–1999. Positive (negative) zonal wave numbers indicate eastward (westward) traveling component relative to ground. Dotted lines denote ground-based eastward phase speed.

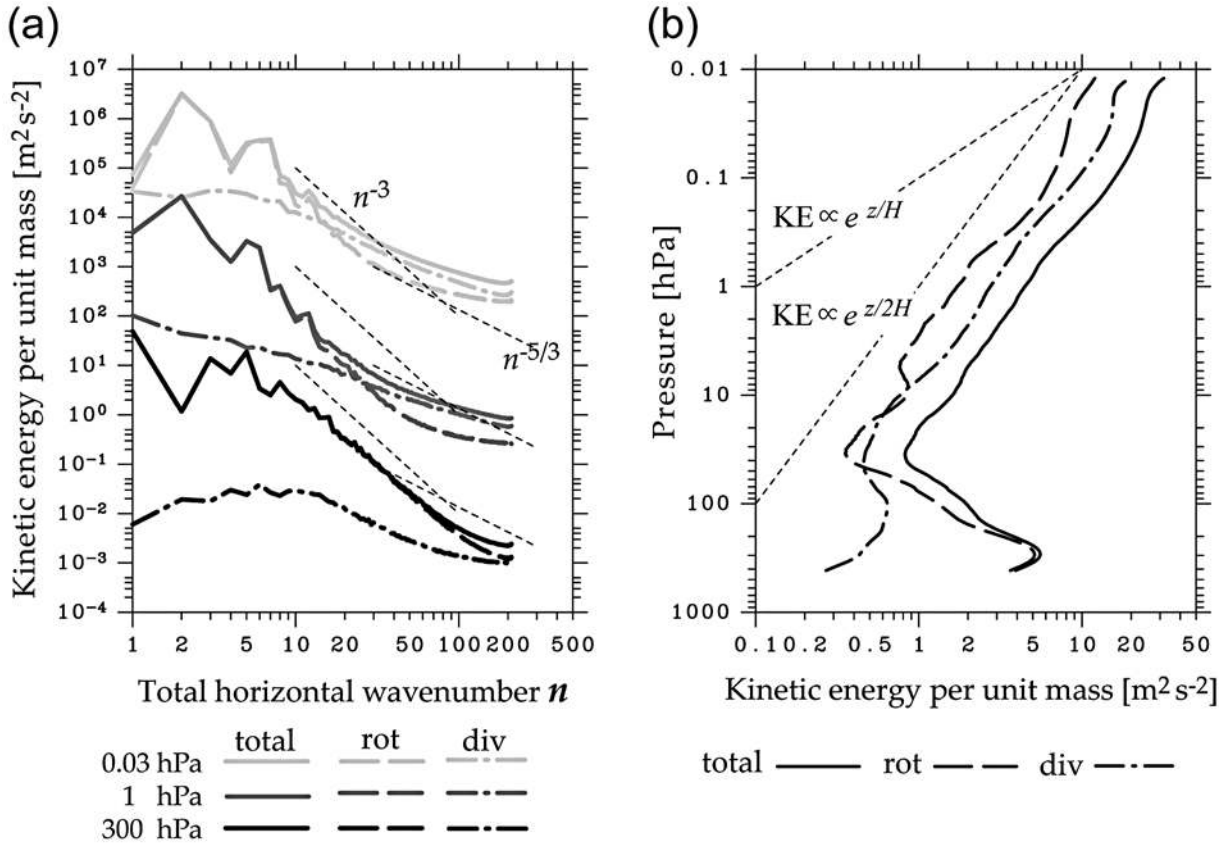

Figure 6. (a) Total horizontal wave number spectra of horizontal kinetic energy. Results at 1 hPa and 0.03 hPa are multiplied by 100 and 10000, respectively. (b) Vertical profile of horizontal kinetic energy integrated over n = 16–213 shown as an average over 1–10 January.

to overestimation of the strength of the Southern Hemisphere subtropical westerly jet (≈+5 m s^{-1}) (see Figure 1), which is seen throughout the year. Such a westerly bias is a common problem for other versions of the CCSR/NIES/FRCGC AGCM and MIROC, and the cause has yet to be understood.

3.4. Horizontal Wave Number Spectra of Kinetic Energy

[37] Figure 6a shows the total horizontal wave number (n) spectra for horizontal kinetic energy (KE) per unit mass, as examined in the model intercomparison study by *Koshyk et al.* [1999]. The rotational and divergent components are calculated separately following the method of *Koshyk et al.* [1999], and the summation of components is displayed as a total component. These components are calculated at 300, 1, and 0.03 hPa, and averaged over the period of 1–10 January. At 300 hPa in the upper troposphere, the spectrum has an approximate slope of n^{-3} at n = 15–50, gradually becoming shallower as n increases from 50 to 70 and approaching the $n^{-5/3}$ slope at n = 70–120. This trend is consistent with observations by commercial aircraft at middle latitudes [*Nastrom et al.*, 1984]. The spectral slope becomes shallower than that of the observations at n > 120, where the divergent component has large KE comparable to that of the rotational component. As the divergent component roughly corresponds to gravity waves, the shallow spectral slope at n > 120 may indicate overestimation of gravity wave energy in the upper troposphere of the GCM, probably due to the horizontal diffusion setting (see section 2.5). The divergent component of KE at large n becomes large with increasing altitude, and the slope becomes shallower in the stratosphere and mesosphere. Such a vertical variation in spectral shape is qualitatively similar to that produced by the GFDL SKYHI GCM [*Koshyk et al.*, 1999].

[38] Figure 6b shows vertical profiles of KE for the rotational, divergent, and total components. The profiles are calculated and integrated over n = 16–213 after subtraction of the zonal mean fields from the original data. The KEs of both the rotational and divergent components have maxima in the upper troposphere, are lower in the lower stratosphere, and then increase from about 30 hPa to the upper mesosphere. The rotational component is dominant in the troposphere and lower stratosphere, while the divergent component exceeds the rotational component above 50 hPa. Straight lines with slopes of +1 and +1/2 in the log-log plot of KE versus inverse pressure are shown in Figure 6, corresponding to altitude variations of KE $\propto e^{z/H}$ and KE $\propto e^{z/2H}$, respectively. An exponential decrease in atmospheric density with height should cause KE to vary in rough proportion to $e^{z/H}$. However, the slope of total KE is close to the KE $\propto e^{z/2H}$ line above 40 hPa, indicating that approximately half of the wave energy is dissipated in the GCM. Such a vertical variation in KE is qualitatively

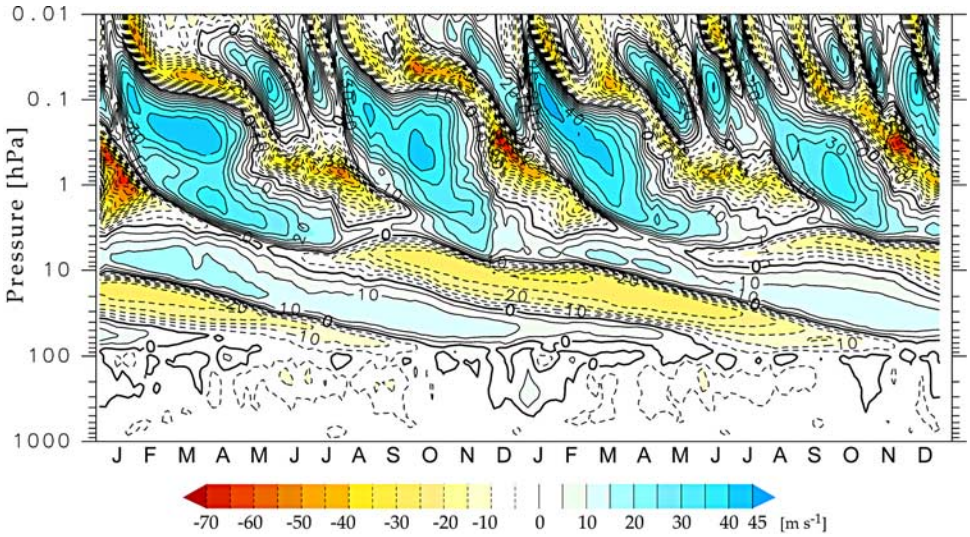

Figure 7. Temporal evolution of 6-day mean zonal mean zonal wind at the equator.

similar to that produced by the SKYHI GCM [*Koshyk et al.*, 1999].

3.5. Equatorial Zonal Wind

[39] Figure 7 shows the evolution of vertical profiles of the zonal mean zonal wind at the equator during the first and second simulation years. Alternating downward propagation of easterly and westerly winds is seen in the lower stratosphere, yielding a structure similar to the equatorial QBO [*Baldwin et al.*, 2001]. The QBO-like oscillation in the GCM has a period of approximately 15 months, which is roughly half of that for the real QBO (≈28 months). The reasons for this short period are currently under investigation. The vertical structure of the zonal mean zonal wind is realistic, with the westerlies maximum reaching 15 m s^{-1}, and the easterlies maximum reaching −25 m s^{-1} at 30 hPa. The westerly shear zone, below which the easterlies are replaced with the descending westerlies, experiences greater vertical shear than the easterly shear zone. The lower extension of the QBO-like oscillation, corresponding to the base of the westerly wind at 80 hPa, is realistic, as are the meridional extension (Figure 1) and the speed of the tropical upwelling in the lower stratosphere (not shown). Further analysis on the zonal momentum budget associated with the QBO-like oscillation is currently underway, and will be reported in the near future.

[40] The S-SAO is realistically simulated by the present GCM [cf. *Garcia et al.*, 1997], reproducing the reversals of zonal wind from easterlies to westerlies in the mesosphere, with the westerlies gradually descending with time. The westerly to easterly reversals occur more rapidly in the lower mesosphere. The S-SAO first cycle in the year involves a large-amplitude zonal mean zonal wind. The easterlies and westerlies maxima in the lower mesosphere are approximately −70 m s^{-1} and 35 m s^{-1} in the first cycle, and close to −50 m s^{-1} and 35 m s^{-1} in the second cycle. A companion paper by *Tomikawa et al.* [2008] describes the generation mechanism of strong meridional circulation appearing in the easterly wind of the S-SAO in the model. An intraseasonal oscillation with period of 30–60 days appears in the middle and upper mesosphere, as observed in the T63L250 simulation [*Watanabe and Takahashi*, 2005]. Such an oscillation might be associated with intraseasonal oscillation in the troposphere [e.g., *Miyoshi and Fujiwara*, 2006], which is beyond the scope of the present study.

3.6. Wave Mean Flow Interactions

[41] The wave mean flow interactions in the GCM were investigated by Eliassen and Palm (E-P) flux analysis [e.g., *Andrews et al.*, 1987] with the aim of evaluating the relative importance of various kinds of atmospheric waves on maintenance of the large-scale zonal wind structures in the middle atmosphere. For this purpose, the wave components are separated into three groups in terms of horizontal wave number. The first group, planetary waves (PW), is defined as the zonal wave number (s) 1–3 component, and is extracted by FFT. Extratropical planetary waves and large-scale equatorial Kelvin waves are included in the PW group. The second group, medium-scale waves (MW), is defined as the total horizontal wave number (n) 1–42 component, excluding $s = 1–3$, and is extracted by spherical filtering using the Legendre transformation. Spherical filtering is more preferable for the present study than the conventional FFT in the zonal direction, because we are focusing on three dimensionally propagating atmospheric waves. The conversion procedure from the gridded fields to the spherical harmonics is identical to that used in the present GCM, and avoids aliasing effects. The MW group consists of waves with horizontal wavelengths longer than 950 km, excluding planetary waves. Synoptic-scale waves, sub-synoptic-scale waves, and large-scale (and probably low-frequency) gravity waves are included in the MW group. Equatorial Rossby-gravity waves are also classified as belonging to the MW group. The third group, with $n \geq 43$, is mostly due to small-scale gravity waves (GW), and is extracted using a spherical high-pass filter. The horizontal wavelengths of the GW group are in the range of 188–930 km. The GW group is not simulated in most climate models with T42 horizontal resolution. Hence, the characteristics of the GW wave group may provide useful information for the development of better gravity wave drag

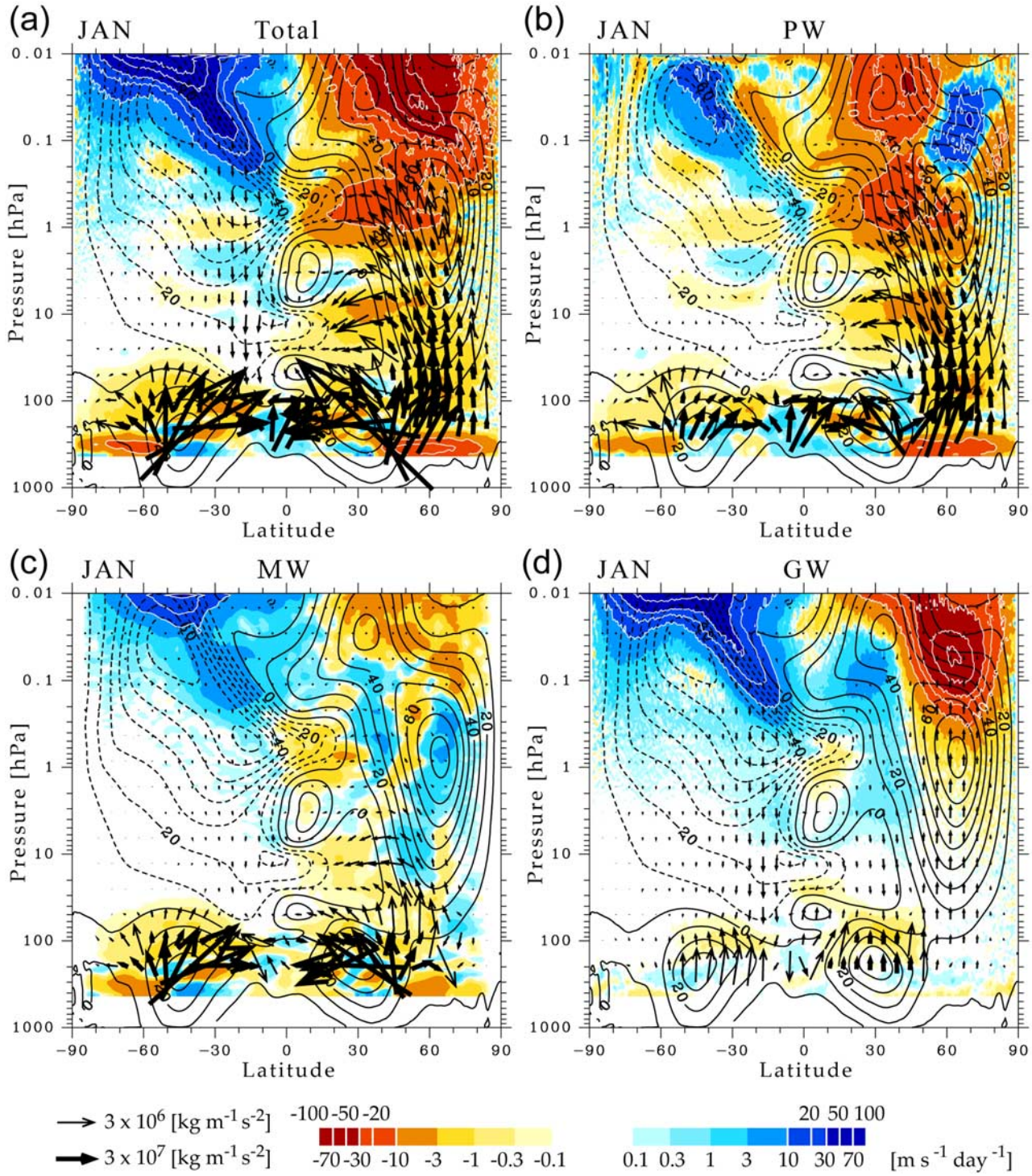

Figure 8. E-P flux vectors (arrows) and eastward accelerations of zonal mean zonal wind due to divergence of E-P flux (colors) for January (average). (a) Total wave components, (b) PW group, (c) MW group, and (d) GW group. Vertical component of E-P flux is multiplied by 250. Scales of arrows are modified for clarity, depending on magnitude of E-P flux. Color scale is logarithmic. Contours denote zonal mean zonal wind in 10 m s^{-1} intervals.

parameterizations [e.g., *Watanabe et al.*, 2008; S. Watanabe, Constraints on a non-orographic gravity wave drag parameterization using a gravity wave resolving general circulation model, submitted to *Scientific Online Letters on the Atmosphere*, 2008].

[42] Figure 8 shows meridional cross sections of the E-P flux vectors and the zonal wind accelerations obtained from divergence of the E-P flux. Results are shown separately for the total wave components, and the PW, MW, and GW

wave groups. The cross sections for the PW group (Figure 8b) show that extratropical planetary waves propagate upward through the low-latitude side of the polar night jet. As the extratropical planetary waves propagate equatorward and approach the zero wind line of the zonal mean zonal wind, the E-P flux converges, and a corresponding westward acceleration of the zonal mean zonal wind occurs. The contribution of planetary waves explains most of the total westward accelerations in the midlatitude middle stratosphere and in the low-latitude and midlatitude lower mesosphere. The westward acceleration in the latter region exceeds -10 m s^{-1} d^{-1}, and is important in production of the easterly phase of the S-SAO.

[43] The results for the GW group (Figure 8d) reveal two regions in which the E-P flux is large; in the Northern Hemisphere polar vortex, and in the Southern Hemisphere subtropics. The upward E-P flux in the Northern Hemisphere polar night jet represents the upward flux of westward momentum, which is likely to be due to gravity waves propagating westward relative to the mean wind. The breaking of gravity waves causes strong deceleration of the polar vortex in the mesosphere (≈ -80 m s^{-1} d^{-1}), which explains most of the decelerations due to the total wave components, and determines the form of the westerly wind in the mesosphere. The downward E-P flux in the Southern Hemisphere subtropics represents the upward flux of eastward momentum, which is likely to be attributable to gravity waves propagating eastward relative to the mean wind. Gravity wave breaking causes strong deceleration of the easterly wind ($>+20$ m s^{-1} d^{-1}) above the center of the summer easterly jet, which explains most of the deceleration due to the total wave components. The E-P flux is small in the middle atmosphere of the Southern Hemisphere at middle and high latitudes, and decelerations of the easterly jet occur at higher altitudes than in the subtropics.

[44] In the tropical lower stratosphere, the E-P flux due to the GW group is divergent in easterly shears associated with the QBO-like oscillation and the S-SAO, and is convergent in westerly shears. The zonal momentum budget analysis around the equatorial stratopause is discussed by *Tomikawa et al.* [2008]. In the midlatitude lower stratosphere, the upper part of the subtropical jet decelerates because of the dissipation of gravity waves. The maximum deceleration is approximately 3 m s^{-1} d^{-1} near 35°N and 100 hPa, where orographic gravity waves and nonorographic gravity waves may coexist. Similar deceleration is also seen around the Southern Hemisphere subtropical jet (see also Figure 9d for July).

[45] The results for the MW group (Figure 8c) indicate that large E-P fluxes in the tropospheric subtropical jets are likely to be associated with baroclinic waves, which do not propagate far into the middle atmosphere. In the mesosphere, the divergence and convergence of E-P flux produce substantial but smaller zonal wind accelerations than those associated with the other two wave groups. In the Southern Hemisphere extratropics, a 30 m s^{-1} d^{-1} deceleration of the mesospheric easterly jet is seen, which explains roughly one third of the total deceleration. Such a deceleration is probably caused by the dissipation of large-scale gravity waves.

[46] Figure 9 shows the corresponding E-P flux diagnostics for July. The results for the PW group (Figure 9b) show that extratropical planetary waves propagate upward and equatorward through the Southern Hemisphere polar vortex. The convergence of the E-P flux associated with the extratropical planetary waves explains most of the total E-P flux convergence, that is, deceleration of the zonal mean westerlies, around the center and low-latitude side of the polar vortex.

[47] The results for the GW group (Figure 9d) indicate that in the Southern Hemisphere lower stratosphere, the upward E-P flux has a weak bimodal structure, with peaks at 40–50°S and 65–75°S. A group of gravity waves in the midlatitude region propagates upward and poleward, and breaks in the mesosphere mainly in the region of 50–60°S, causing strong deceleration of the zonal mean westerly wind. This strong deceleration (≈ -90 m s^{-1} d^{-1}) dominates the total E-P flux convergence in the mesosphere, and is important in maintaining the meridional structure of the polar vortex. The other group of gravity waves in the high-latitude region propagates upward, and starts to dissipate in the upper stratosphere. This group contains orographic gravity waves previously pointed out by *Watanabe et al.* [2006].

[48] The summertime easterly wind in the middle atmosphere of the Northern Hemisphere during July has a similar structure to that in the Southern Hemisphere during January (see Figure 8d). The summertime meridional distribution of the gravity wave E-P flux and wind deceleration are also similar in the Northern and Southern Hemispheres, although the magnitude of the E-P flux is larger in the Northern Hemisphere summer subtropics. Such hemispheric differences are probably due to a strong easterly flow in the upper troposphere of the Northern Hemisphere summer subtropics, which is associated with the Indian summer monsoon circulation. The strong easterly flow filters most of the westward traveling gravity waves, and allows eastward traveling gravity waves to propagate upward into the stratosphere [*Watanabe et al.*, 2008; Watanabe, submitted manuscript, 2008]. As in January, the MW group (Figure 9c) has a substantial but smaller contribution to the total E-P flux divergence in the mesosphere in July.

[49] The E-P flux diagnostics highlight the importance of extratropical planetary waves and small-scale gravity waves with respect to zonal wind accelerations in the stratosphere and mesosphere, respectively. The relative importance of the wave groups to tropical circulations such as the QBO-like oscillation and the S-SAO, is studied in separate papers [e.g., *Tomikawa et al.*, 2008].

3.7. Meridional Propagation of Gravity Waves

[50] The E-P flux analyses for the GW group (small-scale gravity waves) reveal a number of new features. The meridional distribution of the gravity wave drag in the mesosphere depends on the distribution of gravity wave activity in the lower stratosphere. The upward and westward propagating gravity waves are dominant in the winter polar vortices, while the upward and eastward propagating gravity waves are dominant in the summer subtropics (see Figures 8d and 9d). There are, however, two latitudinal regions in which the E-P flux associated with gravity waves is quite small. The first such region is in the vicinity of the equator, where critical level filtering with phase speeds in the range of zonal wind associated with the QBO-like oscillation

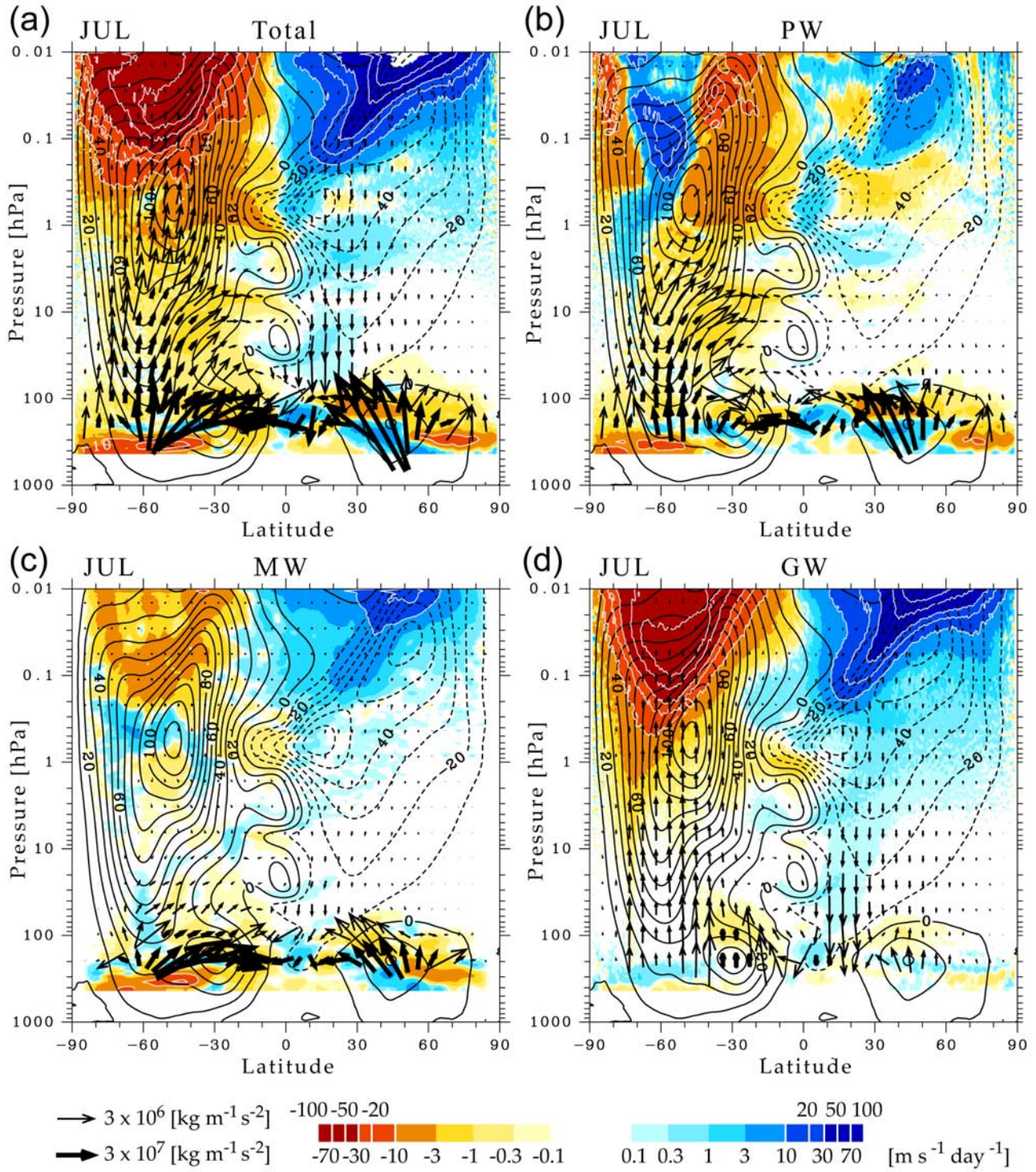

Figure 9. E-P flux vectors (arrows) and eastward accelerations of zonal mean zonal wind due to divergence of E-P flux (colors) for July (average). (a) Total wave components, (b) PW group, (c) MW group, and (d) GW group. Vertical component of E-P flux is multiplied by 250. Scales of arrows are modified for clarity, depending on magnitude of E-P flux. Color scale is logarithmic. Contours denote zonal mean zonal wind in 10 m s^{-1} intervals.

inhibits the upward propagation of gravity waves. The other region is the summer midlatitude and high-latitude region, suggesting the importance of critical level filtering by the westerlies in the troposphere and lower stratosphere. The weak E-P flux in the summer high latitudes also suggests a lack of strong wave sources. These meridional distributions are qualitatively consistent with gravity wave characteristics obtained by satellite measurements [*Wu and Waters*, 1996; *Tsuda et al.*, 2000; *Ern et al.*, 2004; *Alexander et al.*, 2008]. However, as satellite sensors measure different quantities

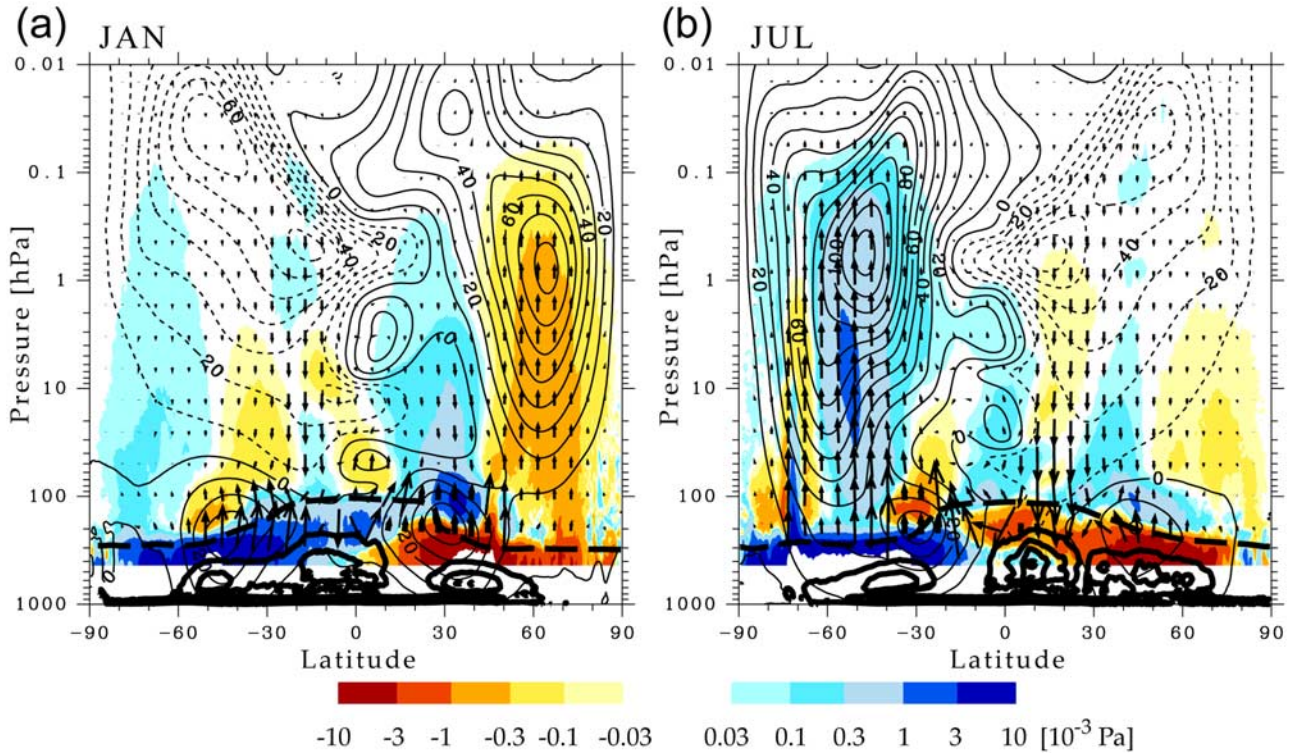

Figure 10. Zonal mean vertical flux of meridional momentum ($\rho_0\overline{v'w'}$) associated with $n \geq 43$ waves (color) and zonal mean zonal wind (contours) in (a) January and (b) July. Arrows denote corresponding E-P flux as shown in Figures 8d and 9d. Bold dashed line denotes the tropopause, and solid contour lines denote monthly average values of zonal mean condensational heating rate in the troposphere (cumulus + large-scale condensation, contour interval of 1 K d^{-1}).

using limited field of views and sensitivity (weighting) functions [*Alexander*, 1998], the results of the present model will need to be validated against satellite data by applying appropriate observational filter functions. Further research in this area is currently being planned.

[51] Figure 10 shows the vertical flux of meridional momentum due to small-scale ($n \geq 43$) gravity waves. The contours for the zonal mean zonal wind and the E-P flux vectors shown in Figures 8d and 9d are superimposed for comparison. The dominant meridional directions of wave propagation are inferred from the meridional momentum flux. The dominant propagation direction of gravity waves is generally consistent with the meridional directions of the E-P flux vectors. The locations of dominant wave sources are also inferred from the meridional momentum flux in the lower stratosphere, since gravity waves generally propagate away from the source. Strong sources exist on the poleward side of the winter subtropical jet, in the tropics and summer subtropics, and around the summer subtropical jet. These locations correspond to regions of large condensational heating release in the troposphere, and are characterized by vertical motions associated with convection, and dynamical instabilities associated with surface fronts and jet streams, which may also generate gravity waves.

[52] The upward E-P flux vectors in Figure 10 indicate differences in the meridional propagation of the westward propagating gravity waves in the polar vortices of the Northern Hemisphere and the Southern Hemisphere. In January of the second year of the simulation, the polar vortex is confined to the northern high latitudes, and westward propagating gravity waves generated around the subtropical jet only propagate marginally into the polar vortex (Figure 10a), instead being dissipated in the lower stratosphere upon reaching critical levels. The large zonal asymmetry of the zonal wind in January is also likely to affect the propagation and generation of gravity waves in the northern high latitudes. In July, the polar vortex in the lower stratosphere has broader latitudinal extent than that in January, and the westward propagating gravity waves generated at middle latitudes propagate upward and poleward, well into the polar vortex (Figure 10b). The E-P flux vectors and the peak of the meridional momentum flux clearly tilt poleward with increasing altitude, indicating poleward propagation of gravity waves by as much as 10° latitude from 40–50°S in the lower stratosphere to 50–60°S in the upper stratosphere. As mentioned in section 3.6, such poleward propagation of midlatitude gravity waves is important in terms of the meridional distribution of gravity wave drag in the mesosphere, and with respect to maintenance of the Southern Hemisphere polar vortex (Figure 9d).

[53] Figure 11 shows a snapshot of the meridional cross section for unfiltered horizontal wind divergence ($\nabla_h \cdot v_h$) at 140°E, along with the background zonal wind consisting of $n = 0$–42 components. The snapshot is taken at the start of July (0000 Coordinated Universal Time (UTC) on 1 July). Although the wave and zonal wind fields are highly complex, the dominant source locations and meridional propagation of individual gravity waves are generally con-

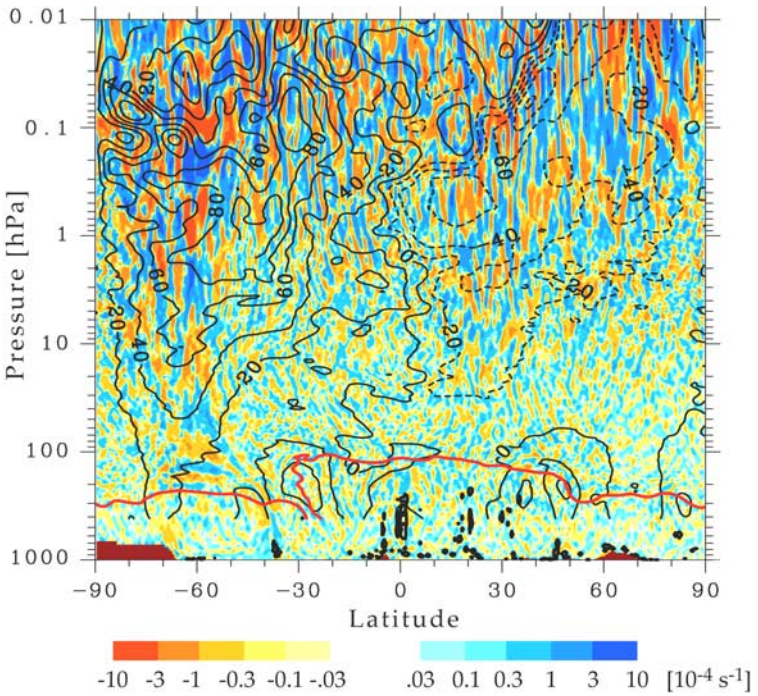

Figure 11. Meridional cross section of unfiltered instantaneous horizontal wind divergence (colors in logarithmic scale) and background (n = 0–42) zonal wind (contours) at 140°E on 1 July (0000 UTC). Bold red line denotes the tropopause. Thick solid contour lines denote condensational heating rate in the troposphere (cumulus + large-scale condensation, contour interval of 1 K d^{-1}). Contours of zonal wind and tropopause height are suppressed below 400 hPa because the horizontal spherical low-pass filter is unavailable because of topography. Surface topography is indicated in brown.

sistent with those shown in Figures 9d and 10b. Figure 11 also reveals that tropical deep convection which occurs near the equator generates V-shaped gravity wave patterns starting near the tropopause and propagating both northward and southward. Similar V-shaped propagation patterns are obvious over the Northern Hemisphere subtropical jet (48°N), although no strong convection occurs at this moment of this longitude. Some of these wave patterns reach the polar region or the subtropics above approximately 10 hPa. The meridional propagation of gravity waves is clearest in regions of weak background zonal wind, where the dominant gravity waves have short vertical wavelengths and large horizontal group velocities. In the polar night jet and the summer easterly jet, gravity waves have longer vertical wavelengths (λ_z > 10 km) due to the Doppler shift associated with strong wind. The Doppler shift effect simultaneously increases the vertical group velocity of gravity waves, resulting in weaker horizontal propagation.

3.8. Case Studies of Gravity Wave Generation

[54] Two characteristic gravity wave phenomena reproduced by the present GCM are described here and compared with observations and the results of other modeling studies. Gravity waves are represented by unfiltered horizontal wind divergence (see Figure 11) with respect to a background field consisting of n = 0–42 components.

3.8.1. Orographic Gravity Waves Over South Andes

[55] Figure 12a shows maps of horizontal wind divergence and background zonal wind at 30 hPa. A clear gravity wave pattern is produced over the southern Andes Mountains, the phase lines of which are aligned approximately parallel to the north-south aligned surface ridge. The background westerlies in the vicinity of the wave region is weak (15–25 m s^{-1}) compared to that to the west (25–30 m s^{-1}), suggesting the possible effect of gravity waves on background flows; that is, momentum deposition due to dissipation of the gravity waves may cause decelerations of the background flows. Figure 12b shows a longitude-pressure cross section of the horizontal wind divergence and potential temperature at 35°S for comparison with the distribution of the tropopause, surface topography, and moist heating, and Figure 12c shows a vertical profile of the background zonal wind. Two different wave phase structures can be identified in Figure 12b, both of which are gravity waves propagating westward relative to the mean westerlies. The first is an orographic gravity wave propagating upward above and downstream of the surface ridge, while the other is a nonorographic gravity wave probably generated by moist heating upstream of the surface ridge. The nonorographic gravity wave has shorter horizontal wavelength (≈210 km) than the orographic gravity wave (≈245 km), and is dominant upstream of the surface ridge. Part of the nonorographic gravity wave may interact with the preexisting orographic gravity wave above the surface ridge. Both waves have similar vertical wavelengths (≈6.4 km), and both propagate upward through the polar night jet, penetrating into the mesosphere. Clear overturning of potential temperature surfaces and regions of Ri < 0.25 are observed in the mesosphere, and other regions of Ri < 0.25 are apparent in the lower stratosphere. The breaking of the

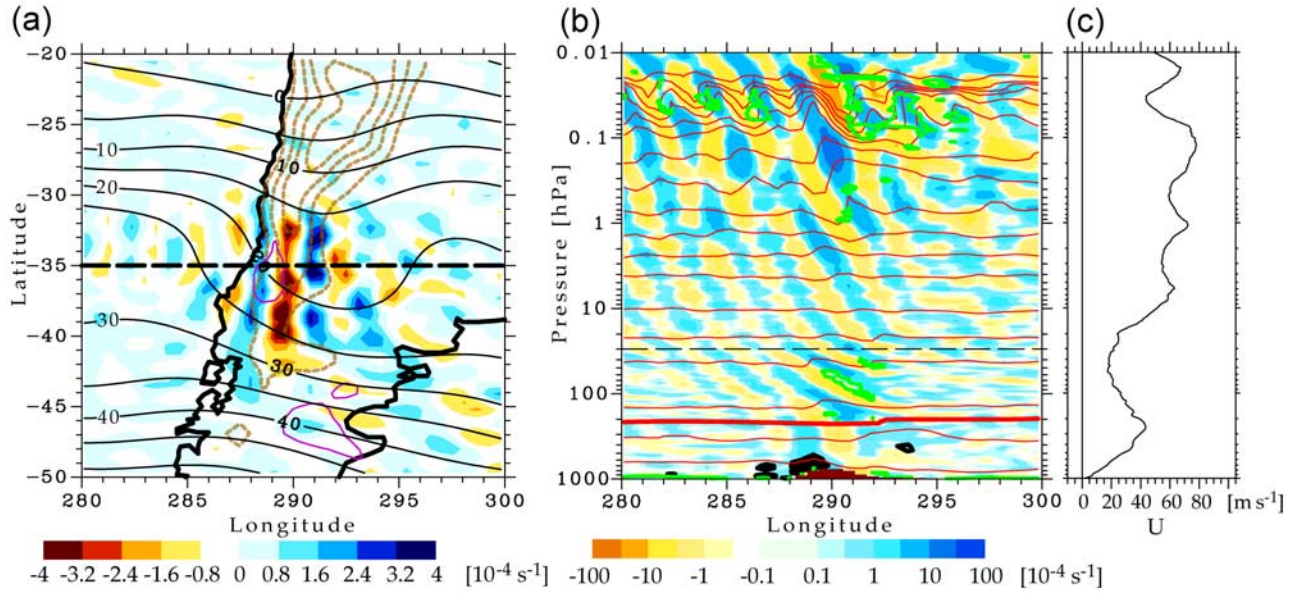

Figure 12. (a) Divergence of unfiltered horizontal wind (color) and background ($n = 0-42$) zonal wind (black contour lines) at 30 hPa on 5 July (1000 UTC). Brown dotted lines denote contours of surface topography in the model with the interval of 1000 m. Pink lines denote 1 mm h^{-1} contours of precipitation. Bold dashed line denotes 35°S. (b) Divergence of unfiltered horizontal wind (color, logarithmic scale) and unfiltered potential temperature (red lines) at 35°S. Bold red line near 200 hPa denotes the tropopause. Regions enclosed by green lines have $Ri < 0.25$. Thick black contours denote condensational heating rate in the troposphere (cumulus + large-scale condensation, contour interval of 0.5 K h^{-1}). Brown denotes the surface topography at 290°E. Horizontal dashed line denotes 30 hPa. (c) Background zonal wind at 35°S averaged over 280–300°E.

gravity waves causes deceleration of the background westerlies, corresponding to the regions of weak wind in the vertical wind profile (Figure 12c).

[56] The wave parameters for the gravity waves are summarized in Table 1. The intrinsic wave frequency ($\hat{\omega}$), ground-based zonal phase speed (c_x), and vertical group velocity (c_{gz}) are estimated using the dispersion relation for gravity waves [cf. *Fritts and Alexander*, 2003]. The parameters are estimated for the lower stratosphere (30–80 hPa), where the vertical wind shear of the polar night jet is small. These gravity waves have short horizontal wavelengths, although the wavelengths remain substantially longer than the minimum resolved horizontal wavelength of the GCM (≈188 km). The gravity waves have small zonal phase speeds relative to the ground ($|c_x| < 1.8$ m s^{-1}) and high intrinsic frequencies ($|f/\hat{\omega}| < 0.15$). The vertical wavelength and vertical group velocity of the gravity waves increase rapidly with height in the upper stratosphere and mesosphere because of Doppler shift associated with the background wind shear.

[57] *Eckermann and Preusse* [1999] described similar westward propagating orographic gravity waves around the Patagonian Andes Mountains (40–50°S) based on CRISTA temperature data. The gravity waves reported by *Eckermann and Preusse* [1999] are similar in vertical wavelength to the present orographic gravity waves, and both vertical wavelengths are consistent with that theoretically predicted for stationary mountain waves: $\lambda_z \approx 2\pi U/N$ or $\lambda_z \approx 6$ km for the present case in the lower stratosphere, close to the 6.4 km value determined by wave phase analysis. Clear orographic gravity wave structures have also been reported over the Patagonian Andes Mountains through the combination of vertical profiles of temperature along orbital tracks of HIRDLS [*Alexander et al.*, 2008]. The amplitude of temperature fluctuations associated with the orographic gravity waves in that case is 5–8 K in the lower stratosphere, similar to the fluctuations associated with the present orographic gravity wave (not shown). Comparison of orographic gravity waves produced by the GCM with those obtained by satellite measurements is useful for validating GCM results, and such validations will be performed in the future for other geographical locations. It is also interesting to investigate the effects of such orographic gravity waves on large-scale circulations through the use of a GCM [e.g., *Watanabe et al.*, 2006].

Table 1. Wave Parameters for Orographic (ORO) and Nonorographic (NORO) Gravity Waves Examined in Figure 12[a]

	λ_x (km)	λ_z (km)	$\lvert f/\hat{\omega}\rvert$	c_x (m s^{-1})	c_{gz} (km h^{-1})	U[b] (m s^{-1})	N[c] (s^{-1})
ORO	245	6.4	0.15	−1.6	2.0	20.0	0.0211
NORO	210	6.4	0.13	+1.8	2.3	23.1	0.0209

[a]The wave parameters are estimated in (35°S, 289–292°E, 30–80 hPa) for ORO, and (35°S, 282–286°E, 30–80 hPa) for NORO, respectively.
[b]Background zonal wind (average in vicinity of gravity waves).
[c]Brunt-Väisälä frequency (average in vicinity of gravity waves).

3.8.2. Gravity Waves Around the Subtropical Jet

[58] Figure 13 show a series of maps of horizontal wind divergence at 100 hPa over the North Atlantic, at time points of 1800, 2200 and 2500 UTC on 4 January. An upper level cold trough can be seen developing over the North Atlantic. The wind maximum of the subtropical jet, as indicated by the 50 m s^{-1} isotach, occurs between the cold trough and a ridge upstream of the trough (32°N, 324°E in

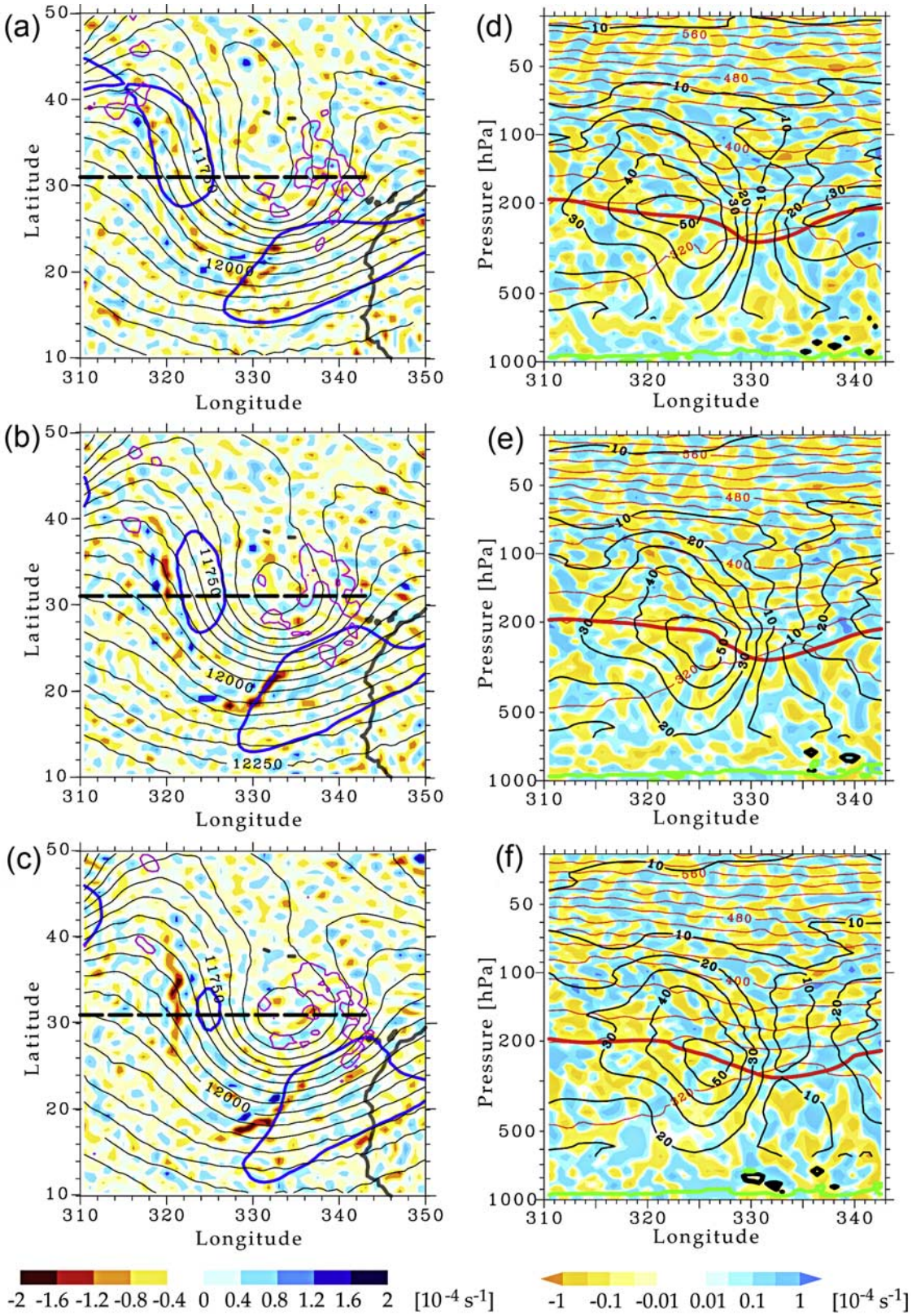

Figure 13

Table 2. Wave Parameters for Upward (JETup) and Downward (JETdw) Propagating Gravity Waves Examined in Figure 13e[a]

	λ_x (km)	λ_z (km)	$\lvert f/\hat{\omega}\rvert$	c_x (m s^{-1})	c_{gz} (km h^{-1})	U[b] (m s^{-1})	N[c] (s^{-1})
JETup	262	2.2	0.42	+8.0	0.18	15.4	0.0196
JETdw	262	2.9	0.63	+4.7	−0.13	9.8	0.0087

[a]The wave parameters are estimated in (31°N, 320–327°E, 200–100 hPa) for JETup, and (31°N, 320–327°E, 500–200 hPa) for JETdw, respectively.
[b]Background zonal wind (average in vicinity of gravity waves).
[c]Brunt-Väisälä frequency (average in vicinity of gravity waves).

Figure 13b). A gravity wave is apparent on the west side of this wind maximum, with approximately north–south wave phase lines aligned parallel to the meandering subtropical jet. The corresponding longitude–pressure cross sections for horizontal wind divergence and horizontal wind speed along the 31°E line are also shown in Figure 13. An interesting feature revealed by these cross sections is the eastward movement of the subtropical jet, and the emission of pairs of upward and downward propagating gravity waves near the core of the jet, as indicated by the change in the vertical phase tilt above and below the jet core. The gravity waves propagate behind the eastward moving subtropical jet in a manner resembling the bow waves from a ship.

[59] The wave parameters estimated for the upward and downward propagating gravity waves in Figure 13e are summarized in Table 2. The two gravity waves have similar horizontal wavelength of about 262 km. The upward propagating gravity wave has shorter vertical wavelength and higher intrinsic frequency in the stratosphere compared with the downward propagating gravity waves in the troposphere, probably because of larger background wind speeds and larger static stability in the stratosphere. The ground-based eastward phase speed of the gravity wave in the stratosphere is approximately +8 m s^{-1}, slightly slower than the speed of the eastward moving jet core (≈+8.6 m s^{-1}) observed in Figure 13e. The ground-based eastward phase speed of the gravity wave in the troposphere is approximately +4.7 m s^{-1}. The phase lines of the gravity wave thus move eastward with the jet core in the stratosphere, and trail the jet core in the troposphere. The gravity wave in the stratosphere disappears at close to 70 hPa as it approaches its critical level.

[60] *Hirota and Niki* [1986] and *Sato* [1994] observed similar upward and downward propagating gravity waves near the subtropical jet by using the MU radar, a very high frequency (VHF) radar located in Shigaraki, Japan (34.9°N, 136.1°E). It was shown in *Sato* [1994] that the gravity waves propagate southward from the poleward side of the zonally elongated subtropical jet. Although the present subtropical jet is oriented north–south, the gravity waves obviously originate on the polar (high potential vorticity) side of the subtropical jet. In this sense, the generation mechanism for the simulated gravity wave appears to be similar to that for comparable observed gravity waves. The wave parameters derived from the observation are also very similar to the present results. The source mechanism for the gravity wave revealed in Figure 13 appears not to be associated with topographical or convective generation. One possible generation mechanism is a spontaneous adjustment process in the vicinity of the subtropical jet or instability in the surrounding fields [e.g., *Tateno and Sato*, 2008]. During the period illustrated in Figure 13, the wind maximum of the subtropical jet moves eastward at a speed of up to 8–9 m s^{-1}. The pressure gradient rapidly increases with time on the east side of the subtropical jet, which can be expected to disrupt the maintenance of geostrophic balance. The possibility of such dynamical instability and the mechanisms of gravity wave generation remain to be investigated in detail.

[61] A number of numerical studies have been performed with the aim of resolving the spontaneous generation of gravity waves during idealized life cycles of baroclinic instability [e.g., *O'Sullivan and Dunkerton*, 1995; *Plougonven and Snyder*, 2007]. The synoptic pattern for the present case resembles that described in *O'Sullivan and Dunkerton* [1995], although the complete cutoff of the cold vortex that occurs in their simulation is not apparent here. The gravity waves simulated by *O'Sullivan and Dunkerton* [1995] occur upstream of an upper level cold trough, and some have similar horizontal phase structures to those described in the present study. However, the wave structure resolved by the longitude–height cross sections differ from those obtained in the present study. In the simulation of *O'Sullivan and Dunkerton* [1995], the gravity waves appear well above the core of the jet stream, and the phase lines of which are aligned approximately parallel to the tropopause, indicating that generation mechanism of gravity waves in that case, suggested to be related to horizontal deformation of the jet stream, differs from that in the present case. In a simulation by *Kawatani et al.* [2004] using the T106L60 version of the CCSR/NIES/FRCGC AGCM, gravity waves were found to develop around the southern winter subtropical jet. The wave phase structures resolved in the longitude–height cross sections are similar to those identified in present study. The vertical wavelengths are also comparable with those presented here, although the horizontal wavelength (λ_x) is substantially longer than in the present study (600–700 km versus 262 km). The intrinsic frequency normalized with respect

Figure 13. (a–c) Horizontal distribution of unfiltered horizontal wind divergence at 100 hPa (color), background geopotential height (black contour lines), 50 m s^{-1} isotach (blue contour lines) at 200 hPa, and precipitation (pink contour lines, interval of 1 mm h^{-1}). (d–f) Longitude-pressure cross section at 31°N (bold dashed line in Figures 13a–13c) for unfiltered horizontal wind divergence (color, logarithmic scale), background absolute wind speed (black contour lines), unfiltered potential temperature (red contour lines), condensational heating rate (bold black contour lines), $Ri = 0.25$ (green contour lines), tropopause (bold red lines). Figures 13a and 13d are for 4 January, 1800 UTC; Figures 13b and 13e are for 4 January, 2200 UTC; and Figures 13c and 13f are for 4 January, 2500 UTC.

to the local inertial frequency ($|\hat{\omega}/f|$) is also similar between the two studies (present, 2.4; *Kawatani et al.* [2004], 2.1). Idealized simulations of baroclinic wave life cycles by *Plougonven and Snyder* [2007] produced many kinds of gravity waves, suggesting the existence of a range of source mechanisms associated with the upper level jet streams and surface fronts. They also showed that both the wave parameters and amplitude of the waves forced changed with changing spatial resolution. Further case studies will be necessary in order to investigate the variety of source mechanisms for gravity wave generation in the present GCM.

4. Discussion

[62] The T213L256 middle atmosphere GCM developed in the present study reasonably simulates the meridional structures of the zonal mean zonal wind and zonal mean temperature in January and July (see section 3.1), with the exception that the maximum wind speed of the mesospheric westerly jet (polar night jet) in the Southern Hemisphere winter is overestimated. The results of E-P diagnostics show that deceleration of the mesospheric westerly jet is primarily caused by the dissipation of small-scale gravity waves which propagate westward relative to the mean westerlies (see section 3.6). Hence, it is suggested that the zonal wind drag force due to the dissipation of such gravity waves is insufficient to maintain realistic strength of the mesospheric westerly jet. Otherwise, it may mean that subgrid-scale diffusion processes represented by the horizontal hyperdiffusion and the Richardson number–dependent vertical diffusion parameterization, which strongly affect vertical growth of gravity wave amplitudes, alter altitudes where breakdown of gravity waves occurs. Namely, simulated gravity waves may break at slightly higher altitudes than those in the real atmosphere if the parameterized diffusion is overly strong. The magnitude of the drag force is proportional to the vertical convergence of net vertical flux of zonal momentum associated with gravity waves reaching the mesosphere.

[63] The gravity wave momentum flux in the GCM is dependent on many processes, and the gravity wave characteristics are sensitive to the parameterized source and dissipation mechanisms in the GCM. The horizontal resolution of the GCM also affects not only the total wave energy, but also the wave characteristics and source mechanisms, such as convection, topography, instability, and adjustment processes. Many studies have been conducted to investigate the sensitivities of simulated large-scale circulations on the horizontal resolution of the GCM. Such studies for the middle atmosphere have been performed using the SKYHI GCM [*Miyahara et al.*, 1986; *Hayashi et al.*, 1989; *Jones et al.*, 1997; *Hamilton et al.*, 1999], in which gravity wave drag parameterizations are not employed. It has been found that the maximum wind speed of the polar night jets in both hemispheres decreases with increasing horizontal resolution, while the gravity wave momentum flux increases. *Kawamiya et al.* [2005] reported differences in results obtained using the T106L250 and T213L250 GCMs, with the latter simulating the Southern Hemisphere polar night jet more accurately (overestimated in the T106L250 GCM). The T213L250 GCM produces a gravity wave momentum flux of much greater magnitude than the T106L250 GCM, particularly at Southern Hemisphere middle latitudes and over Antarctica. The T106L250 GCM also failed to reproduce small-scale orographic gravity waves over Antarctica, which were found in simulations using the T213L250 GCM [*Watanabe et al.*, 2006]. Further increases in horizontal resolution may allow the model to resolve small-scale source mechanisms of gravity waves, which are potentially important with respect to large-scale circulations in the middle atmosphere.

[64] The meridional propagation of gravity waves, the importance of which was discussed in section 3.7, has been reported in only a few GCM studies. One of the few examples is the study of *Miyahara et al.* [1986], in which the meridional and horizontal distributions of the vertical flux of zonal momentum obtained by a November simulation of the SKYHI GCM were described. Packets of eastward traveling gravity waves in the tropical midtroposphere were found to propagate upward and southward, reaching the stratosphere and mesosphere in the Southern Hemisphere subtropics. Such characteristics are qualitatively consistent with those revealed by the E-P flux and instantaneous wavefield in the present GCM simulation, although the westerly wind of the QBO-like oscillation observed in the present simulation prevents upward propagation of the eastward traveling gravity waves in the equatorial lower stratosphere.

[65] *Sato et al.* [1999] described the meridional distribution of the vertical flux of meridional momentum associated with short-period (<24 h) gravity waves simulated using an aqua-planet version of the T106L53 CCSR/NIES GCM. The meridional momentum flux in that case has a V-shaped pattern centered in the equatorial midtroposphere, indicating upward and poleward propagation of gravity waves generated primarily in the equatorial middle troposphere. The corresponding meridional structures obtained using the present GCM are more complex (Figure 10). Such differences may be due in part to different filtering techniques (i.e., temporal high-pass filter versus horizontal high-pass filter) used for extracting gravity waves. Some of the differences in the meridional momentum flux distribution are attributable to the generation of the QBO-like oscillation and the realistic bottom boundary conditions in the present GCM. The former will affect wave filtering in the equatorial lower stratosphere, while the latter greatly will modify the large-scale circulations such as monsoon circulations that affect both wave filtering and the distribution of wave sources.

5. Conclusion

[66] In the present study, a T213L256 middle atmosphere GCM developed to study atmospheric gravity waves and the effects of such waves on large-scale fields was presented, and the general characteristics of the model were discussed. The present GCM successfully simulates the spontaneous generation of gravity waves by convection, topography, instability, and adjustment processes, resulting in realistic reproduction of general circulation in the extratropical stratosphere and mesosphere, except for the slight overestimation of the wind speed for the Southern Hemisphere polar night jet in the mesosphere. The meridional distribution of the squared Brunt-Väisälä frequency (N^2)

was also found to be simulated with reasonable accuracy by the T213L256 GCM, including the rapid increase in N^2 above the extratropical tropopause. The mean precipitation was also realistically simulated. The GCM overestimates the zonal phase speed of the upper tropospheric synoptic-scale disturbances in the Southern Hemisphere at middle latitudes, probably because of the westerly wind bias of the subtropical jet. The horizontal wave number spectra for horizontal kinetic energy at 300 hPa have similar logarithmic slopes to observations for the $n < 120$ components, but have shallower slopes compared to observations for the $n > 120$ components. This feature may indicate overestimation of gravity wave energy at large n in the upper troposphere. The vertical variations in the kinetic energy spectra and the integrated wave energies in the present simulation are generally similar to those obtained by the SKYHI GCM. The present GCM generates a spontaneous QBO-like oscillation, although its period (15 months) is approximately half that of the observed QBO. The model also simulates the latitudinal and vertical extensions of the QBO-like oscillation, the vertical wind shear and maximum wind speeds of the easterlies and westerlies, and tropical upwelling with reasonable accuracy. The GCM also simulates the realistic S-SAO including the asymmetry between the easterly and westerly phases.

[67] The relative importance of planetary waves, medium-scale waves, and small-scale gravity waves in terms of the maintenance of large-scale zonal wind structures in the middle atmosphere was investigated by calculating Eliassen-Palm diagnostics separately for each of these three groups of waves. The diagnostics indicate that extratropical planetary waves mainly act to decelerate the equatorward side of the polar vortex below heights of approximately 60 km, while small-scale gravity waves cause deceleration of the wintertime polar night jet and the summertime easterly jet in the mesosphere. The importance of the meridional propagation of gravity waves and the dominant source regions were elucidated by examining the meridional distribution of the meridional momentum flux in reference to a snapshot of the instantaneous horizontal wind divergence. Case studies of orographic gravity waves over the South Andes and gravity waves emitted from the tropospheric jet stream in the GCM were presented. The orographic gravity waves were found to have a realistic wave phase structure and similar temperature fluctuations to observations, and the gravity waves emitted from the tropospheric jet stream were found to be generated by the eastward moving northerly jet upstream of the upper level cold trough and to propagate upward and downward behind the jet.

[68] The T213L256 middle atmosphere GCM was thus shown to realistically reproduce the general circulation in the troposphere, stratosphere, and mesosphere, and to resolve small-scale gravity waves. The results are encouraging, and the present GCM will be employed to conduct further studies as part of the KANTO project. Statistical studies of the global distribution, wave parameters, and propagation characteristics of gravity waves in the GCM are planned, and the GCM results will be compared to recent satellite observations in order to examine the detailed physics included in observed phenomena resolved by observations. These studies will primarily be useful for developing more realistic gravity wave parameterizations by determining constraints that are consistent with observations. It is also of interest to quantify the effects of gravity waves on momentum and thermal balance in the middle atmosphere general circulation. The effects of gravity waves on zonal forcing in January and July were investigated in the present study, and the effects of gravity waves on the seasonal marches of zonal jets, meridional circulations, and thermal structures in the middle atmosphere will be quantified in the near future. The presented high-resolution GCM also represents a useful framework for the study of atmospheric transport processes, particularly in the upper troposphere and lower stratosphere. In this region, large-scale processes (e.g., Brewer-Dobson circulation) and small-scale processes (e.g., irreversible, turbulent mixing) both have a considerable influence on the variation in chemical tracer distributions, particularly those associated with stratosphere-troposphere exchange. The relative roles of the various scales of transport processes in terms of chemical tracer distributions in the tropopause region will be investigated as part of future studies.

[69] **Acknowledgments.** The authors thank anonymous reviewers for their valuable comments on the original manuscript. This work is a contribution to the Innovative Program of Climate Change Projection for the 21st Century supported by the Ministry of Education, Culture, Sports, Science and Technology (MEXT) of Japan. This work was supported by a Grant-in Aid for Scientific Research (19204047) from MEXT, Japan. Calculations were conducted using the Earth Simulator, and figures were prepared using the GFD-DENNOU library and GTOOL.

References

Alexander, M. J. (1998), Interpretations of observed climatological patterns in stratospheric gravity wave variance, *J. Geophys. Res.*, *103*(D8), 8627–8640, doi:10.1029/97JD03325.

Alexander, M. J., and C. Barnett (2007), Using satellite observations to constrain parameterizations of gravity wave effects for global models, *J. Atmos. Sci.*, *64*, 1652–1665, doi:10.1175/JAS3897.1.

Alexander, M. J., et al. (2008), Global estimates of gravity wave momentum flux from High Resolution Dynamics Limb Sounder observations, *J. Geophys. Res.*, *113*, D15S18, doi:10.1029/2007JD008807.

Allen, S. J., and R. A. Vincent (1995), Gravity wave activity in the lower atmosphere: Seasonal and latitudinal variations, *J. Geophys. Res.*, *100*, 1327–1350.

Andrews, D. G., J. R. Holton, and C. B. Leovy (1987), *Middle Atmosphere Dynamics*, 489 pp., Academic, San Diego, Calif.

Arakawa, A., and W. H. Schubert (1974), Interactions of cumulus cloud ensemble with the large-scale environment. Part I, *J. Atmos. Sci.*, *31*, 674–701, doi:10.1175/1520-0469(1974)031<0674:IOACCE>2.0.CO;2.

Baldwin, M. P., et al. (2001), The Quasi-Biennial Oscillation, *Rev. Geophys.*, *39*, 179–229, doi:10.1029/1999RG000073.

Birner, T. (2006), Fine-scale structure of the extratropical tropopause region, *J. Geophys. Res.*, *111*, D04104, doi:10.1029/2005JD006301.

Eckermann, S. D., and P. Preusse (1999), Global measurements of stratospheric mountain waves from space, *Science*, *286*, 1534–1537, doi:10.1126/science.286.5444.1534.

Emori, S., T. Nozawa, A. Numaguchi, and I. Uno (2001), Importance of cumulus parameterization for precipitation simulation over east Asia in June, *J. Meteorol. Soc. Jpn.*, *79*, 939–947, doi:10.2151/jmsj.79.939.

Ern, M., P. Preusse, M. J. Alexander, and C. D. Warner (2004), Absolute values of gravity wave momentum flux derived from satellite data, *J. Geophys. Res.*, *109*, D20103, doi:10.1029/2004JD004752.

Ern, M., P. Preusse, M. Krebsbach, M. G. Mlynczak, and J. M. Russell III (2007), Equatorial wave analysis from SABER and ECMWF temperatures, *Atmos. Chem. Phys. Discuss.*, *7*, 11,685–11,723.

Eyring, V., et al. (2005), A strategy for process-oriented validation of coupled chemistry-climate models, *Bull. Am. Meteorol. Soc.*, *86*, 1117–1133, doi:10.1175/BAMS-86-8-1117.

Eyring, V., et al. (2006), Assessment of temperature, trace species and ozone in chemistry-climate model simulations of the recent past, *J. Geophys. Res.*, *111*, D22308, doi:10.1029/2006JD007327.

Fleming, E. L., S. Chandra, J. J. Barnett, and M. Corney (1990), Zonal mean temperature, pressure, zonal wind, and geopotential height as functions of latitude, COSPAR International Reference Atmosphere: 1986,

part II: Middle atmosphere Models, *Adv. Space Res.*, *10*, 11–59, doi:10.1016/0273-1177(90)90386-E.

Fritts, D. C., and M. J. Alexander (2003), Gravity wave dynamics and effects in the middle atmosphere, *Rev. Geophys.*, *41*(1), 1003, doi:10.1029/2001RG000106.

Garcia, R. R., and B. Boville (1994), "Downward control" of the mean meridional circulation and temperature distribution of the polar winter stratosphere, *J. Atmos. Sci.*, *51*, 2238–2245, doi:10.1175/1520-0469(1994)051<2238:COTMMC>2.0.CO;2.

Garcia, R. R., T. J. Dunkerton, R. S. Lieberman, and R. A. Vincent (1997), Climatology of the semiannual oscillation of the tropical middle atmosphere, *J. Geophys. Res.*, *102*, 26,019–26,032, doi:10.1029/97JD00207.

Hamilton, K., R. J. Wilson, and R. Hemler (1999), Middle atmosphere simulated with high vertical and horizontal resolution versions of a GCM: Improvement in the cold pole bias and generation of a QBO-like oscillation in the tropics, *J. Atmos. Sci.*, *56*, 3829–3846, doi:10.1175/1520-0469(1999)056<3829:MASWHV>2.0.CO;2.

Hayashi, Y., D. G. Golder, J. D. Mahlman, and S. Miyahara (1989), The effect of horizontal resolution on gravity waves simulated by the GFDL "SKYHI" general circulation model, *Pure Appl. Geophys.*, *130*, 421–443, doi:10.1007/BF00874467.

Hirota, I., and T. Niki (1986), Inertia-gravity waves in the troposphere and stratosphere observed by the MU radar, *J. Meteorol. Soc. Jpn.*, *64*, 995–999.

Hitchman, M. H., J. C. Gille, C. D. Rodgers, and G. Brasseur (1989), The separated polar winter stratopause: A gravity wave driven climatological feature, *J. Atmos. Sci.*, *46*, 410–422, doi:10.1175/1520-0469(1989)046<0410:TSPWSA>2.0.CO;2.

Horinouchi, T., et al. (2003), Tropical cumulus convection and upward-propagating waves in middle-atmospheric GCMs, *J. Atmos. Sci.*, *60*, 2765–2782, doi:10.1175/1520-0469(2003)060<2765:TCCAUW>2.0.CO;2.

Huffman, G. J., R. F. Adler, M. M. Morrissey, S. Curtis, R. Joyce, B. McGavock, and J. Susskind (2001), Global precipitation at one-degree daily resolution from multi-satellite observations, *J. Hydrometeorol.*, *2*, 36–50, doi:10.1175/1525-7541(2001)002<0036:GPAODD>2.0.CO;2.

Jones, P. W., K. Hamilton, and R. J. Wilson (1997), A very high-resolution general circulation model simulation of the global circulation in austral winter, *J. Atmos. Sci.*, *54*, 1107–1116, doi:10.1175/1520-0469(1997)054<1107:AVHRGC>2.0.CO;2.

K-1 Model Developers (2004), K-1 coupled GCM (MIROC) description, *K-1 Tech. Rep.*, *1*, pp. 1–34, Univ. of Tokyo, Tokyo, Japan.

Kawamiya, M., C. Yoshikawa, T. Kato, H. Sato, K. Sudo, S. Watanabe, and T. Matsuno (2005), Development of an Integrated Earth System Model on the Earth Simulator, *J. Earth Simulator*, *4*, 18–30.

Kawatani, Y., S. K. Dhaka, M. Takahashi, and T. Tsuda (2003), Large potential energy of gravity waves over a smooth surface with little convection: Simulation and observation, *Geophys. Res. Lett.*, *30*(8), 1438, doi:10.1029/2003GL016960.

Kawatani, Y., M. Takahashi, and T. Tokioka (2004), Gravity waves around the subtropical jet of the southern winter in an atmospheric general circulation model, *Geophys. Res. Lett.*, *31*, L22109, doi:10.1029/2004GL020794.

Kawatani, Y., K. Tsuji, and M. Takahashi (2005), Zonally non-uniform distribution of equatorial gravity waves in an atmospheric general circulation model, *Geophys. Res. Lett.*, *32*, L23815, doi:10.1029/2005GL024068.

Kida, H. (1983), General circulation of air parcels and transport characteristics derived from a hemispheric GCM. Part 1. A determination of advective mass flow in the lower stratosphere, *J. Meteorol. Soc. Jpn.*, *61*, 171–187.

Koshyk, J. N., B. A. Boville, K. Hamilton, E. Manzini, and K. Shibata (1999), Kinetic energy spectrum of horizontal motions in middle atmosphere models, *J. Geophys. Res.*, *104*(D22), 27,177–27,190, doi:10.1029/1999JD900814.

Lawrence, B. N., and W. J. Randel (1996), Variability in the mesosphere observed by the Nimbus 6 pressure modulator radiometer, *J. Geophys. Res.*, *101*(D18), 23,475–23,489, doi:10.1029/96JD01652.

Lin, S.-J., and R. B. Rood (1996), Multidimensional flux-form semi-Lagrangian transport schemes, *Mon. Weather Rev.*, *124*, 2046–2070, doi:10.1175/1520-0493(1996)124<2046:MFFSLT>2.0.CO;2.

Lin, J.-L., et al. (2006), Tropical intraseasonal variability in 14 IPCC AR4 climate models—Part I: Convective signals, *J. Clim.*, *19*, 2665–2690, doi:10.1175/JCLI3735.1.

Matthes, K., Y. Kuroda, K. Kodera, and U. Langematz (2006), Transfer of the solar signal from the stratosphere to the troposphere: Northern winter, *J. Geophys. Res.*, *111*, D06108, doi:10.1029/2005JD006283.

McLandress, C. (1998), On the importance of gravity waves in the middle atmosphere and their parameterization in general circulation models, *J. Atmos. Sol. Terr. Phys.*, *60*, 1357–1383, doi:10.1016/S1364-6826(98)00061-3.

Mellor, G. L., and T. Yamada (1974), A hierarchy of turbulence closure models for planetary boundary layers, *J. Atmos. Sci.*, *31*, 1791–1806, doi:10.1175/1520-0469(1974)031<1791:AHOTCM>2.0.CO;2.

Mellor, G. L., and T. Yamada (1982), Development of a turbulence closure model for geostrophic fluid problems, *Rev. Geophys.*, *20*, 851–875, doi:10.1029/RG020i004p00851.

Miyahara, S., Y. Hayashi, and J. D. Mahlman (1986), Interactions between gravity waves and planetary scale flow simulated by the GFDL "SKYHI" general circulation model, *J. Atmos. Sci.*, *43*, 1844–1861, doi:10.1175/1520-0469(1986)043<1844:IBGWAP>2.0.CO;2.

Miyoshi, Y., and H. Fujiwara (2006), Excitation mechanism of intraseasonal oscillation in the equatorial mesosphere and lower thermosphere, *J. Geophys. Res.*, *111*, D14108, doi:10.1029/2005JD006993.

Naito, Y., M. Taguchi, and S. Yoden (2003), A parameter sweep experiment on the effects of the equatorial QBO on stratospheric sudden warming events, *J. Atmos. Sci.*, *60*, 1380–1394, doi:10.1175/1520-0469(2003)060<1380:APSEOT>2.0.CO;2.

Nakazawa, T. (1988), Tropical super clusters within intraseasonal variations over the western Pacific, *J. Meteorol. Soc. Jpn.*, *66*, 823–839.

Nastrom, G. D., and F. D. Eaton (2006), Quasi-monochromatic inertia-gravity waves in the lower stratosphere from MST radar observations, *J. Geophys. Res.*, *111*, D19103, doi:10.1029/2006JD007335.

Nastrom, G. D., K. S. Gage, and W. H. Jasperson (1984), Kinetic energy spectrum of large-and mesoscale atmospheric processes, *Nature*, *310*, 36–38, doi:10.1038/310036a0.

Nozawa, T., T. Nagashima, T. Ogura, T. Yokohata, N. Okada, and H. Shiogama (2007), Climate change simulations with a coupled ocean-atmosphere GCM called the Model for Interdisciplinary Research on Climate: MIROC, *CGER Supercomput. Monogr. Rep.*, *12*, Cent. for Global Environ. Res., Natl. Inst. for Environ. Stud., Tsukuba, Japan.

O'Sullivan, D., and T. J. Dunkerton (1995), Generation of inertia-gravity waves in a simulated lifecycle of baroclinic instability, *J. Atmos. Sci.*, *52*, 3695–3716, doi:10.1175/1520-0469(1995)052<3695:GOIWIA>2.0.CO;2.

Pawson, S., et al. (2000), The GCM–Reality Intercomparison Project for SPARC (GRIPS): Scientific issues and initial results, *Bull. Am. Meteorol. Soc.*, *81*, 781–796, doi:10.1175/1520-0477(2000)081<0781:TGIPFS>2.3.CO;2.

Plougonven, R., and C. Snyder (2007), Inertia-gravity waves spontaneously generated by jets and fronts. Part I: Different baroclinic life cycles, *J. Atmos. Sci.*, *64*, 2502–2520, doi:10.1175/JAS3953.1.

Randel, W. J., et al. (2004), The SPARC intercomparison of middle-atmosphere climatologies, *J. Clim.*, *17*(5), 986–1003, doi:10.1175/1520-0442(2004)017<0986:TSIOMC>2.0.CO;2.

Sato, K. (1994), A statistical study of the structure, saturation and sources of inertia-gravity waves in the lower stratosphere observed with the MU radar, *J. Atmos. Terr. Phys.*, *56*, 755–774, doi:10.1016/0021-9169(94)90131-7.

Sato, K. (2000), Sources of gravity waves in the polar middle atmosphere, *Adv. Polar Upper Atmos. Res.*, *14*, 233–240.

Sato, K., and T. J. Dunkerton (1997), Estimates of momentum flux associated with equatorial Kelvin and gravity waves, *J. Geophys. Res.*, *102*, 26,247–26,261.

Sato, T., and R. F. Woodman (1982), Fine altitude resolution radar observations of upper-tropospheric and lower-stratospheric winds and waves, *J. Atmos. Sci.*, *39*, 2539–2545.

Sato, K., and M. Yoshiki (2008), Gravity wave generation around the polar vortex in the stratosphere revealed by 3-hourly radiosonde observations at Syowa Station, *J. Atmos. Sci*, in press.

Sato, K., D. J. O'Sullivan, and T. J. Dunkerton (1997), Low-frequency inertia-gravity waves in the stratosphere revealed by three-week continuous observation with the MU radar, *Geophys. Res. Lett.*, *24*, 1739–1742.

Sato, K., T. Kumakura, and M. Takahashi (1999), Gravity waves appearing in a high-resolution GCM simulation, *J. Atmos. Sci.*, *56*, 1005–1018, doi:10.1175/1520-0469(1999)056<1005:GWAIAH>2.0.CO;2.

Sato, K., M. Yamamori, S. Ogino, N. Takahashi, Y. Tomikawa, and T. Yamanouchi (2003), A meridional scan of the stratospheric gravity wave field over the ocean in 2001 (MeSSO2001), *J. Geophys. Res.*, *108*(D16), 4491, doi:10.1029/2002JD003219.

Suzuki, T., Y. N. Takayabu, and S. Emori (2006), Coupling mechanisms between equatorial waves and cumulus convection in an AGCM, *Dyn. Atmos. Oceans*, *42*, 81–106, doi:10.1016/j.dynatmoce.2006.02.004.

Swinbank, R., and A. O'Neill (1994), A stratosphere-troposphere data assimilation system, *Mon. Weather Rev.*, *122*, 686–702, doi:10.1175/1520-0493(1994)122<0686:ASTDAS>2.0.CO;2.

Takahashi, M. (1996), Simulation of the stratospheric quasi-biennial oscillation using a general circulation model, *Geophys. Res. Lett.*, *23*, 661–664, doi:10.1029/95GL03413.

Takahashi, M. (1999), Simulation of the quasi-biennial oscillation in a general circulation model, *Geophys. Res. Lett.*, *26*, 1307–1310, doi:10.1029/1999GL900188.

Tateno, S., and K. Sato (2008), A study of inertia-gravity waves in the middle stratosphere based on intensive radiosonde observations, *J. Meteorol. Soc. Jpn.*, in press.

Tomikawa, Y., K. Sato, S. Watanabe, Y. Kawatani, K. Miyazaki, and M. Takashaki (2008), Wintertime temperature maximum at the subtropical stratopause in a T213L256 GCM, *J. Geophys. Res.*, doi:10.1029/2008JD009786, in press.

Tsuda, T., M. Nishida, C. Rocken, and R. H. Ware (2000), A global morphology of gravity wave activity in the stratosphere revealed by the GPS occultation data (GPS/MET), *J. Geophys. Res.*, *105*, 7257–7273, doi:10.1029/1999JD901005.

Uppala, S. M., et al. (2005), The ERA-40 re-analysis, *Q. J. R. Meteorol. Soc.*, *131*, 2961–3012, doi:10.1256/qj.04.176.

Watanabe, S., and M. Takahashi (2005), Kelvin waves and ozone Kelvin waves in the quasi-biennial oscillation and semiannual oscillation: A simulation by a high-resolution chemistry-coupled general circulation model, *J. Geophys. Res.*, *110*, D18303, doi:10.1029/2004JD005424.

Watanabe, S., S. Miyahara, and Y. Miyoshi (1999), Lagrangian transport experiments in the MLT region, *Earth Planets Space*, *51*, 745–750.

Watanabe, S., T. Hirooka, and S. Miyahara (2002), Interannual variations of the general circulation and polar stratospheric ozone losses in a general circulation model, *J. Meteorol. Soc. Jpn.*, *80*, 877–895, doi:10.2151/jmsj.80.877.

Watanabe, S., T. Nagashima, and S. Emori (2005), Impact of global warming on gravity wave momentum flux in the lower stratosphere, *Sci. Online Lett. Atmos.*, *1*, 189–192, doi:10.2151/sola.2005-049.

Watanabe, S., K. Sato, and M. Takahashi (2006), A general circulation model study of orographic gravity waves over Antarctica excited by katabatic winds, *J. Geophys. Res.*, *111*, D18104, doi:10.1029/2005JD006851.

Watanabe, S., H. Miura, M. Sekiguchi, T. Nagashima, K. Sudo, S. Emori, and M. Kawamiya (2008), Development of an atmospheric general circulation model for integrated Earth system modeling on the Earth Simulator, *J. Earth Simulator*, *9*, 27–35.

Wilson, R., M. L. Chanin, and A. Hauchecorne (1991), Gravity waves in the middle atmosphere observed by Rayleigh lidar: 2. Climatology, *J. Geophys. Res.*, *96*, 5169–5183, doi:10.1029/90JD02610.

Wu, D. (2004), Mesoscale gravity wave variances from AMSU-A radiances, *Geophys. Res. Lett.*, *31*, L12114, doi:10.1029/2004GL019562.

Wu, D. L., and J. W. Waters (1996), Satellite observations of atmospheric variances: A possible indication of gravity waves, *Geophys. Res. Lett.*, *23*, 3631–3634, doi:10.1029/96GL02907.

Yoshiki, M., and K. Sato (2000), A statistical study of gravity waves in the polar regions based on operational radiosonde data, *J. Geophys. Res.*, *105*, 17,995–18,011, doi:10.1029/2000JD900204.

Yoshiki, M., N. Kizu, and K. Sato (2004), Energy enhancements of gravity waves in the Antarctic lower stratosphere associated with variations in the polar vortex and tropospheric disturbances, *J. Geophys. Res.*, *109*, D23104, doi:10.1029/2004JD004870.

Y. Kawatani, K. Miyazaki, M. Takahashi, and S. Watanabe, Frontier Research Center for Global Change, Japan Agency for Marine-Earth Science and Technology, 3173-25 Showa-machi, Kanazawa-ku, Yokohama City, Kanagawa 236-0001, Japan. (wnabe@jamstec.go.jp)

K. Sato, Department of Earth and Planetary Science, Graduate School of Science, University of Tokyo, Tokyo 113-0033, Japan.

Y. Tomikawa, National Institute of Polar Research, Tokyo 173-8515, Japan.